Phasing biology and disease

Literature Seminar

2024/8/5 (Mon)

M2 Yuma Takeuchi

Table of contents

Phasing biology (相分離生物学)

Four classes of protein structure

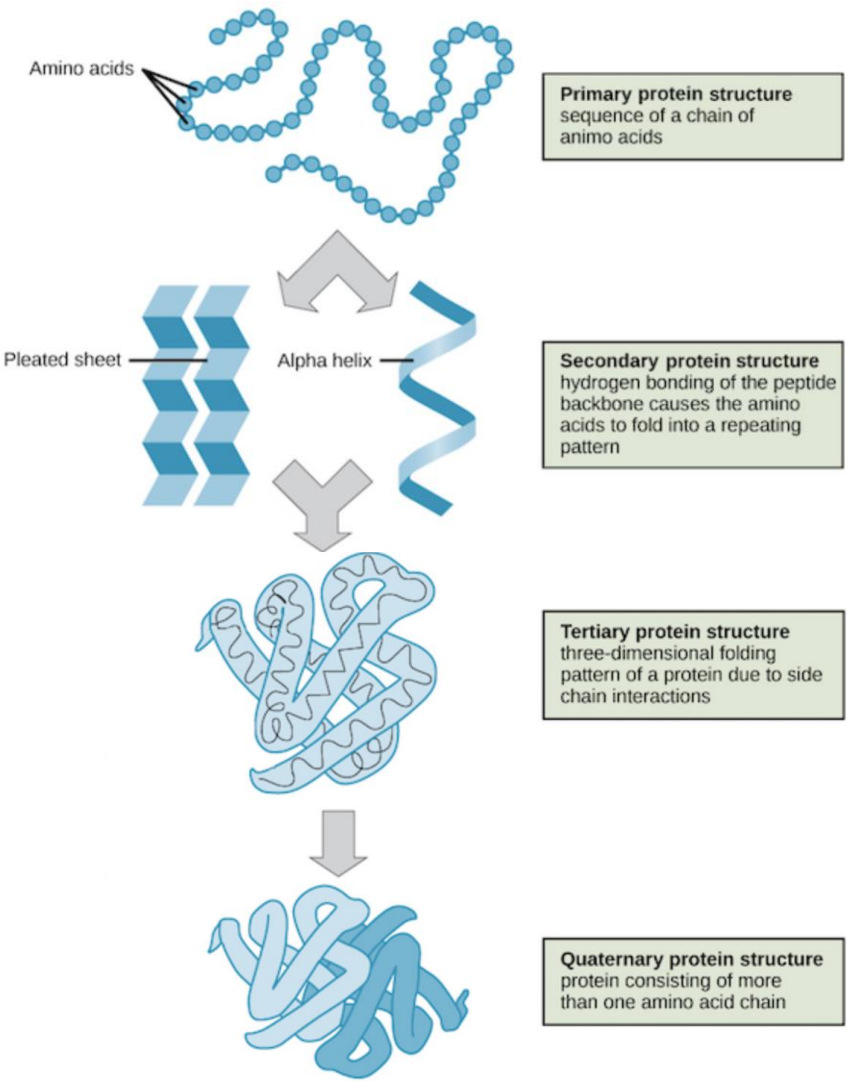

Quinary protein structure (五次構造) (= phase separation structure)

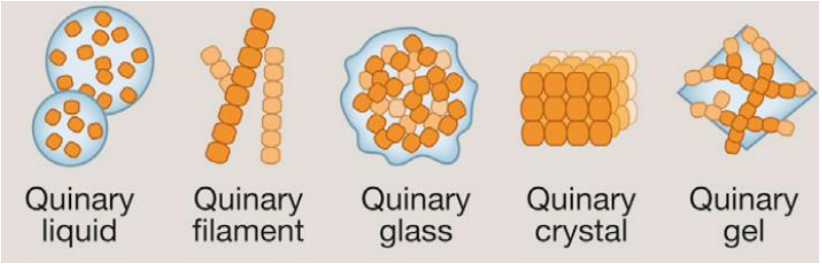

Structure	Main interaction
Primary	Covalent bond
Secondary	Hydrogen bond
Tertiary	Side chain interaction
Quaternary	Protein-Protein interaction (specific, strong)
Quinary	Protein-X interaction (X = Protein, RNA, DNA…) (multivalent, weak)

Kroschwald. S *et al.*, *Cell*, **2017**, *168*, 947-948.

Phasing biology (相分離生物学)

- **Phase separation as a survival strategy**

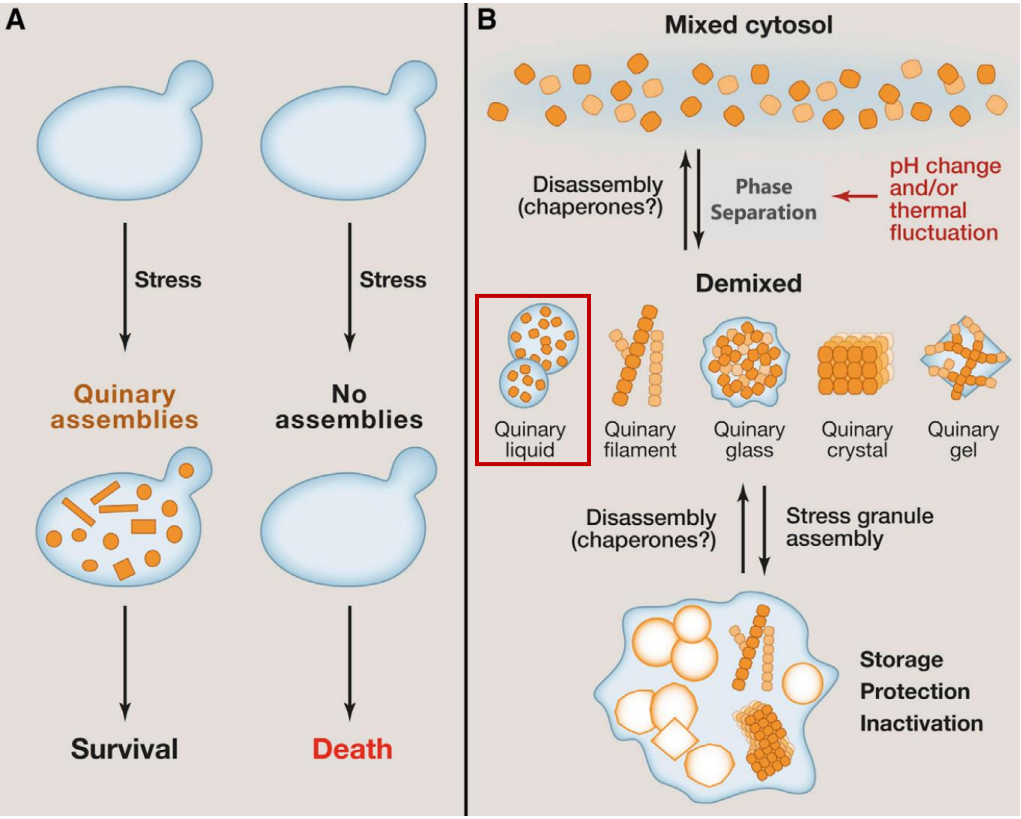

- **Positioning of phasing biology**

	Molecular biology	Structural biology	Phasing biology
Subject	gene product	protein structure	phasing state
Class	primary	tertiary	quinary
Relationship	molecule and function	structure and function	state and function

Kroschwald. S *et al.*, *Cell*, **2017**, *168*, 947-948.

Phasing biology (相分離生物学)

Liquid-Liquid Phase Separation (LLPS) in biology

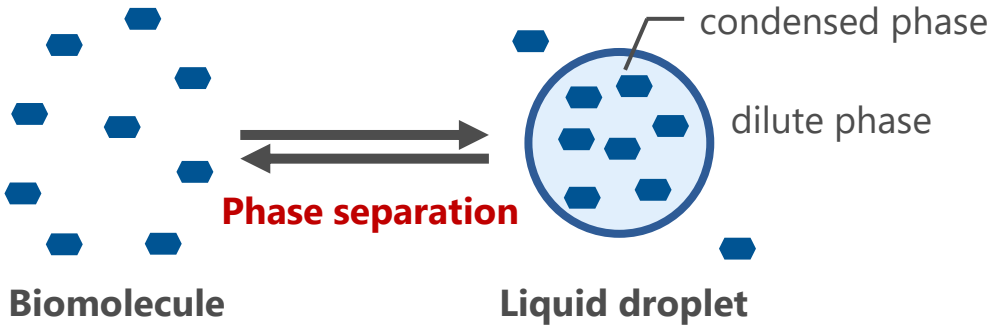

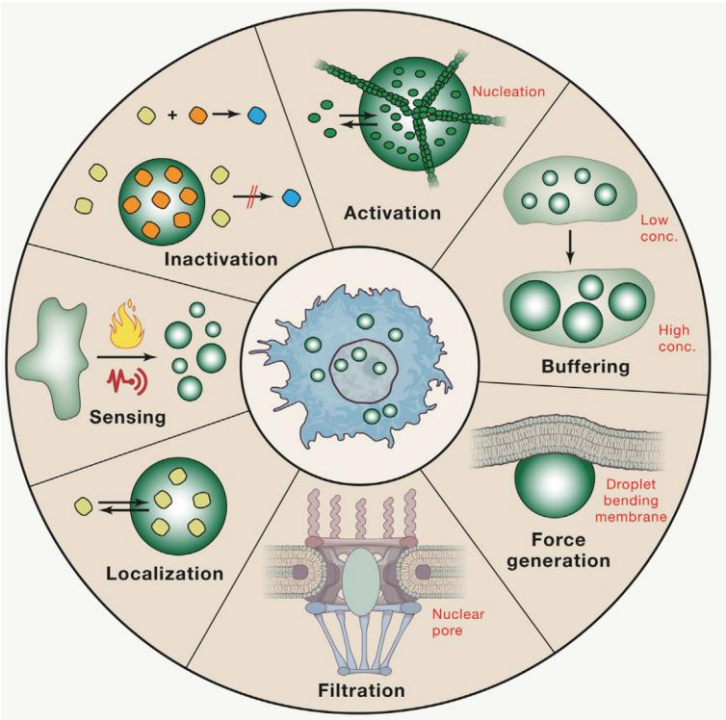

Wang. B *et al.*, *Sig. Transduct. Target Ther.*, **2021**, *6*, 290. Alberti. S *et al. Cell*, **2019**, *176*, 419-434.

Factors driving biological LLPS

IDP (Intrinsically Disordered Protein, 天然変性タンパク質)

IDR (天然変性領域)

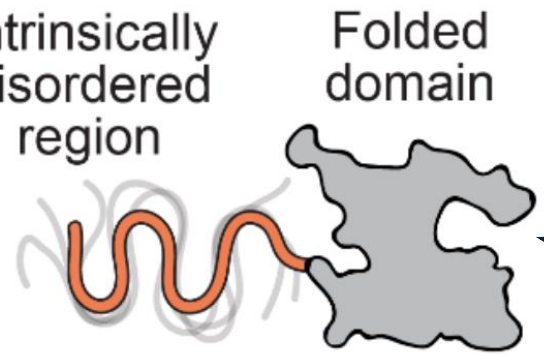

Hydrophilic residues (for interaction)

Hydrophobic residues (for folding)

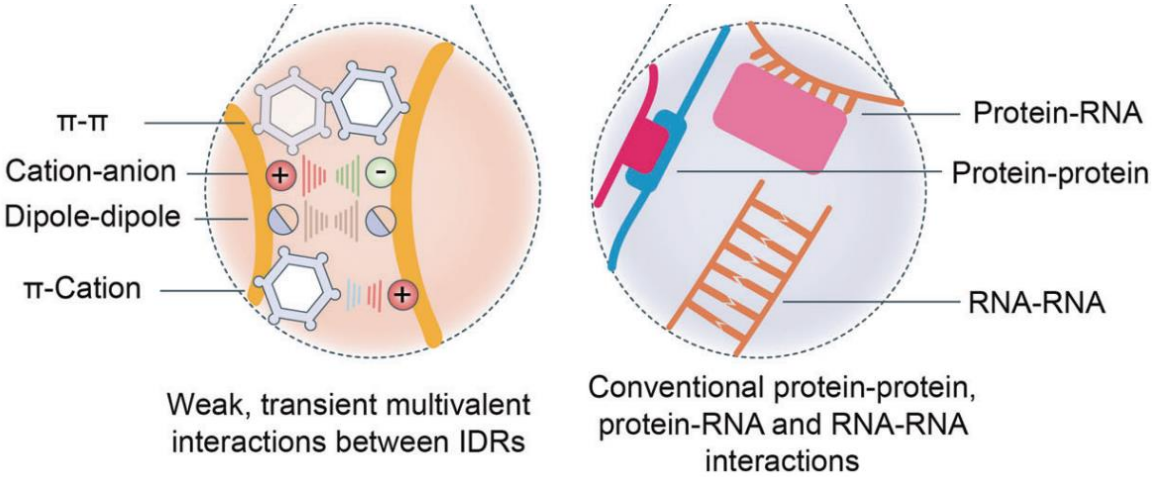

Wang. B *et al.*, *Sig. Transduct. Target Ther.*, **2021**, *6*, 290.

History of the discovery and development of biological LLPS

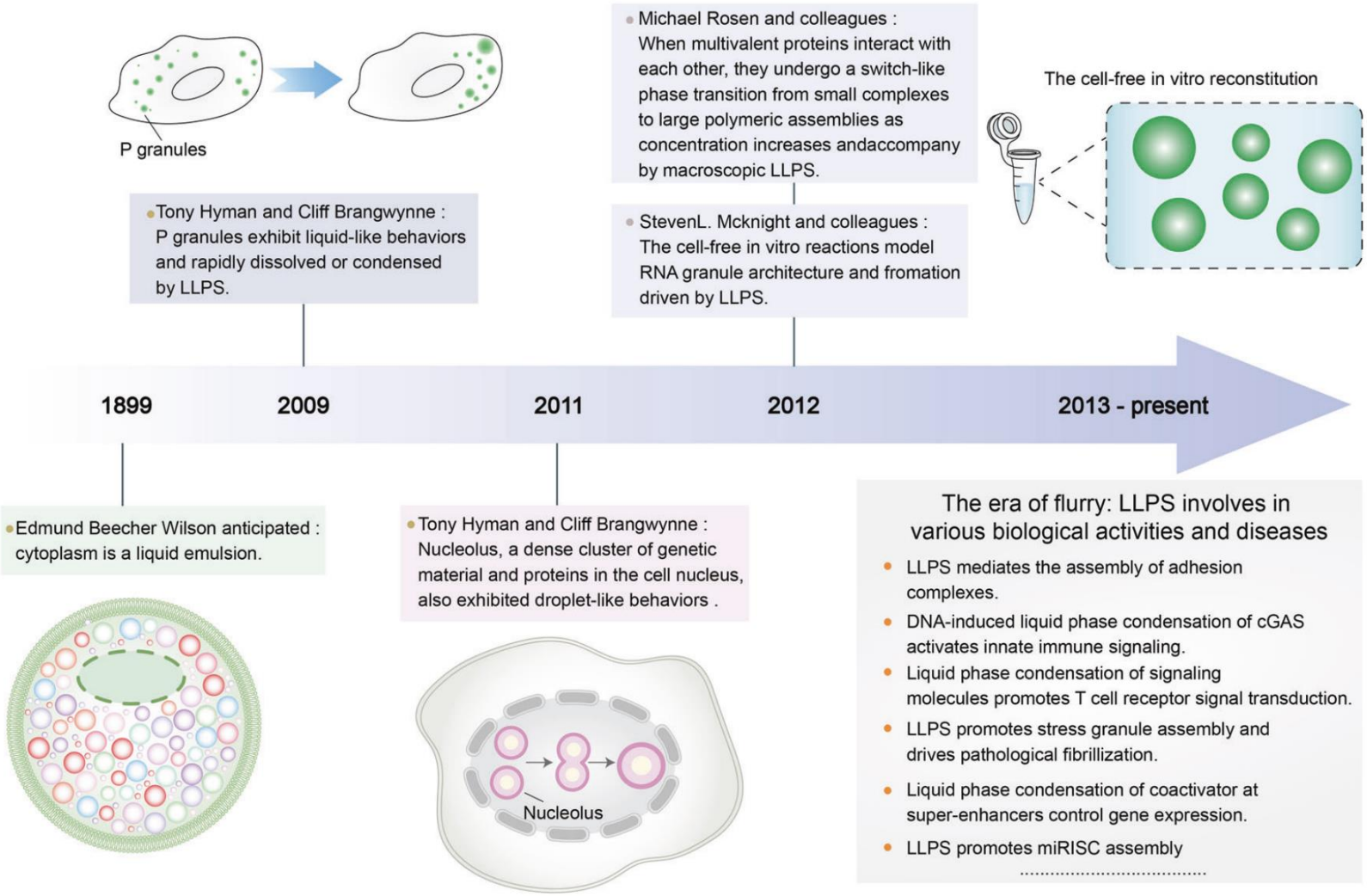

Wang. B *et al.*, *Sig. Transduct. Target Ther.*, **2021**, *6*, 290.

Continuous enzyme reaction

Metabolic pathway map

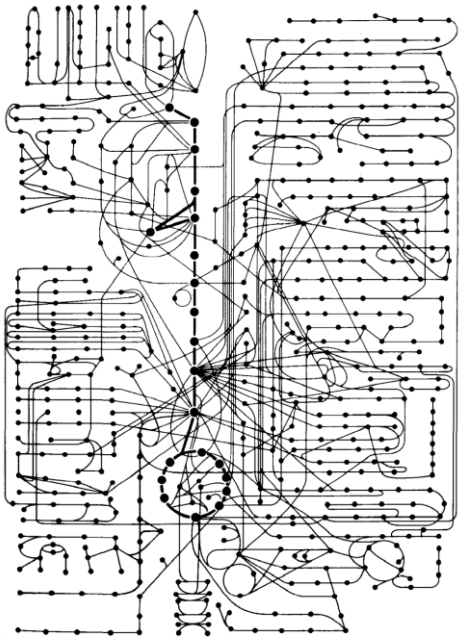

LLPS = reaction field

P. A. Srere, *Ann Rev. Biochem.*, **1987**, *56*, 89-124.

Theoretical calculation

Continuous enzyme reaction cannot occur if the active sites of two enzymes are >10 nm

M. Castellana et al., *Nat. Biotechnol.*, **2014**, *32*(10), 1011-1018.

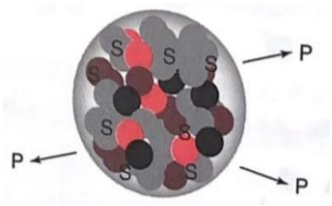

Scheme of continuous enzyme reaction

Substrates, Intermediates, Enzymes: inside droplet

Metabolon: complex of enzymes
Purinosome: complex of purine synthases

HeLa cells
hFGAMS-GFP

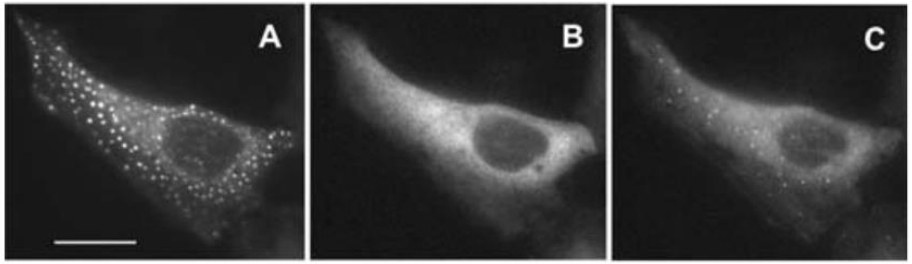

Purine: depleted rich re-depleted

S. An et al., *Science*, **2008**, *320*(5872), 103-106.

Post Translational Modification (PTM)

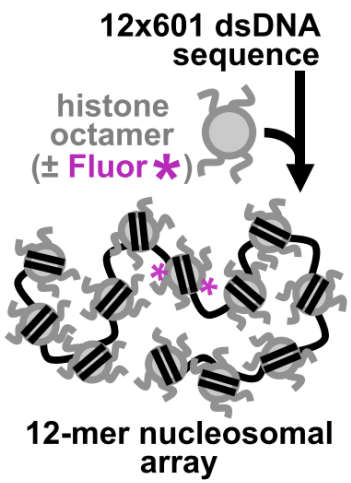

DNA: polyanion
Histone tail: polycation IDR

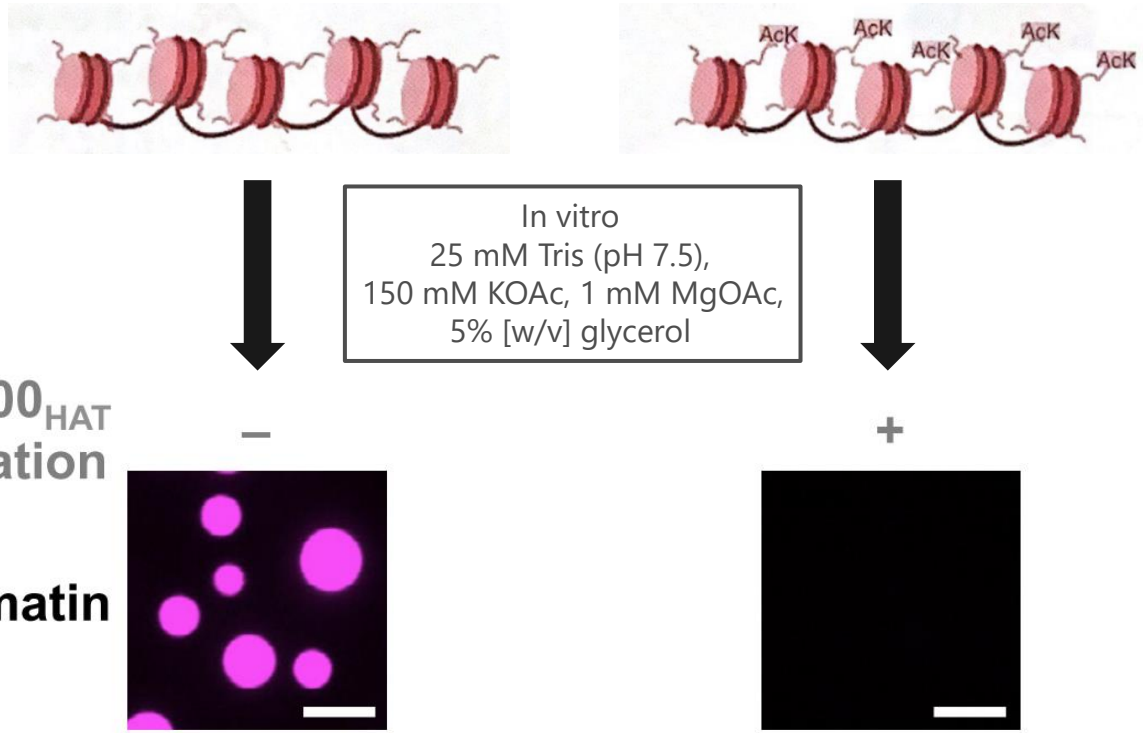

small PTM → change of protein properties (c.f. charge, hydrophilicity) → large LLPS (field)

B. A. Gibson *et al.*, *Cell*, **2019**, 179, 470-484.

RNA sequence, structure and recognition

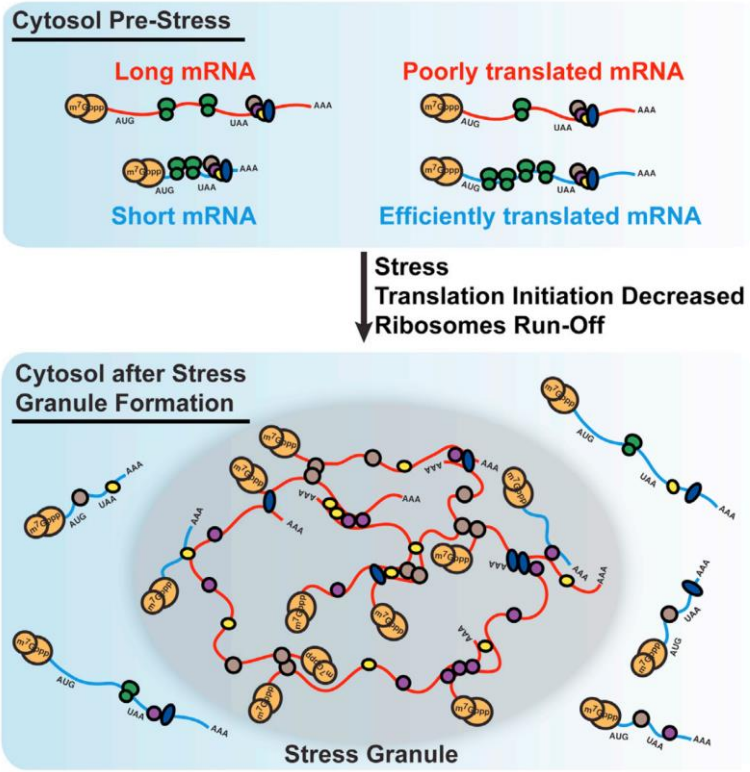

RNA recognition by ribosome

Some mRNAs are enriched in stress granules (>95%) ,while other mRNAs are NOT (<1%)

A. Khong *et al.*, *Mol. Cell*, **2017**, 68(4), 808-820.

Factors driving LLPS (Protein and RNA)

- **RNA sequence and structure**
- **RNA structural change by RNA binding protein**

E. M. Langdon *et al.*, *Science*, **2018**, 360(6391), 922-927.

Importance of RNA tertiary and quinary structure

The capacity of phase separation , as well as amino acid, are coded by mRNA

LLPS and disease

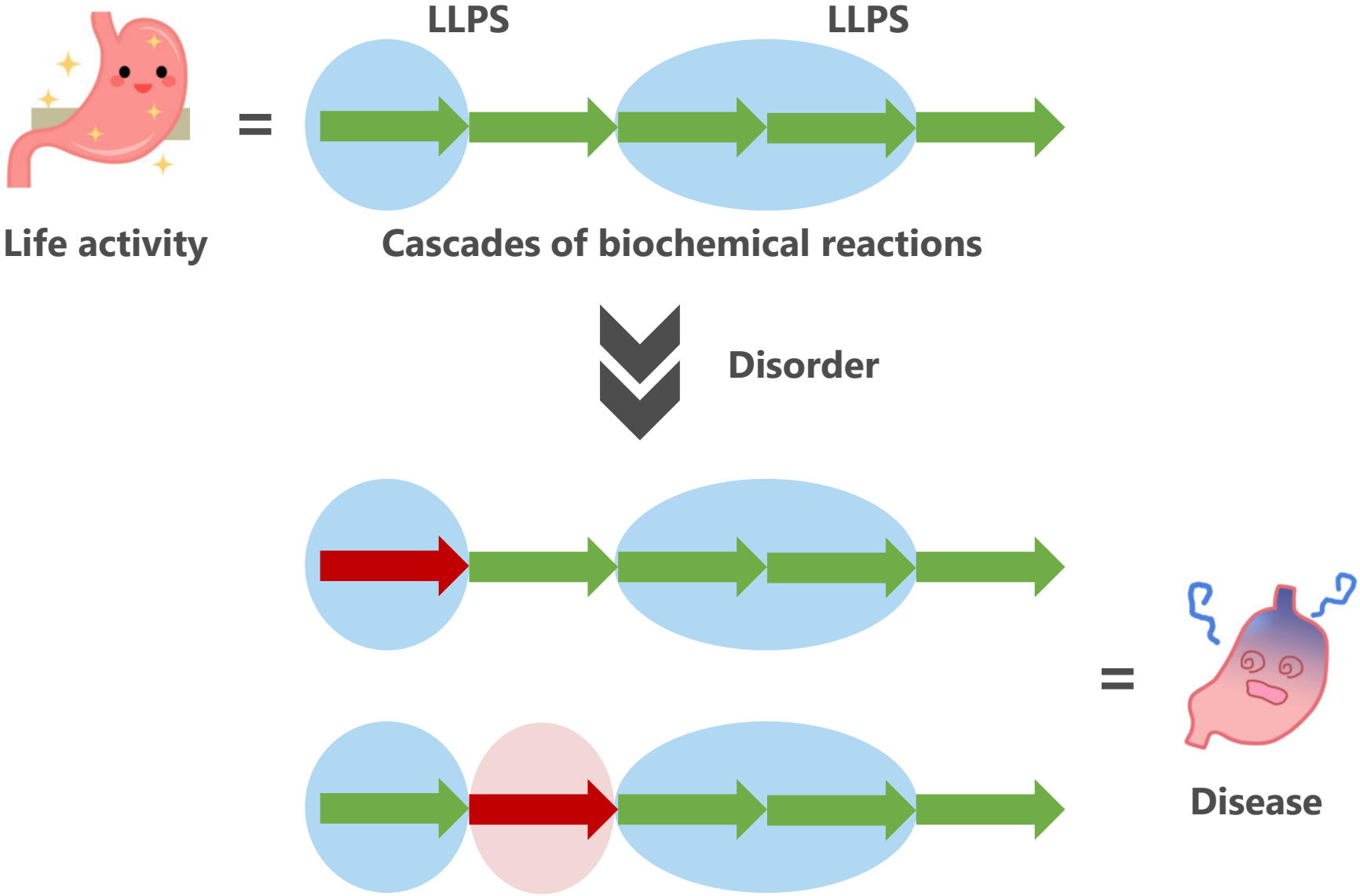

LLPS and disease

Amyloidosis

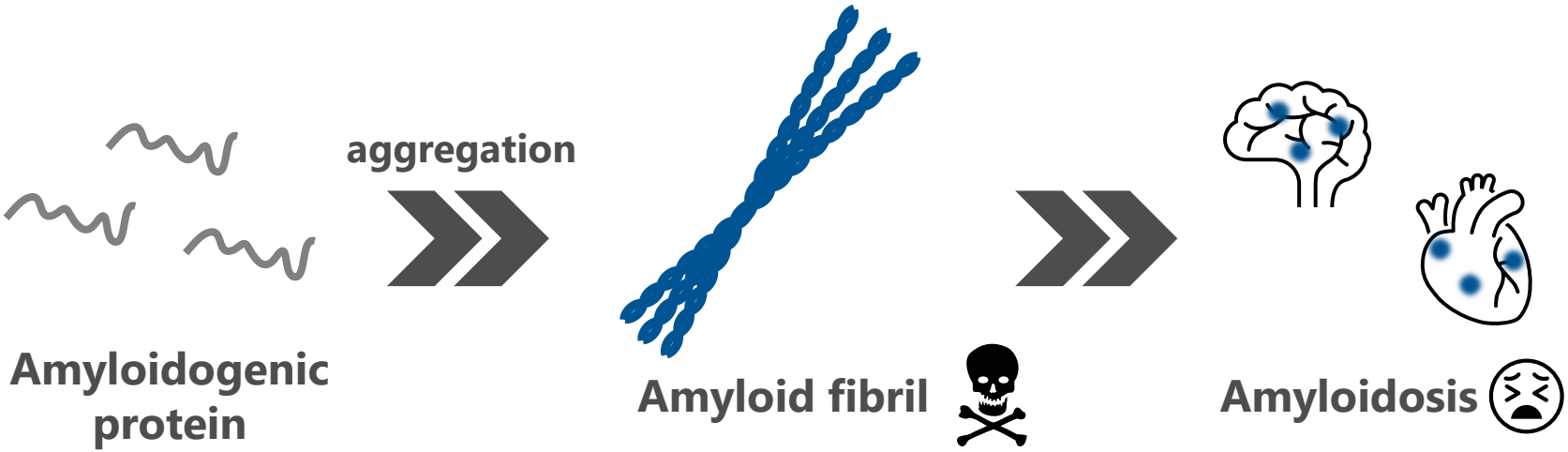

Amyloid-β (Aβ)	Tau
α-synuclein	Transthyretin

Alzheimer disease	
Parkinson disease	TTR amyloidosis

Amyloids are deposited in various organs and cause functional disorder.

LLPS and disease

LLPS and amyloid function (normal)

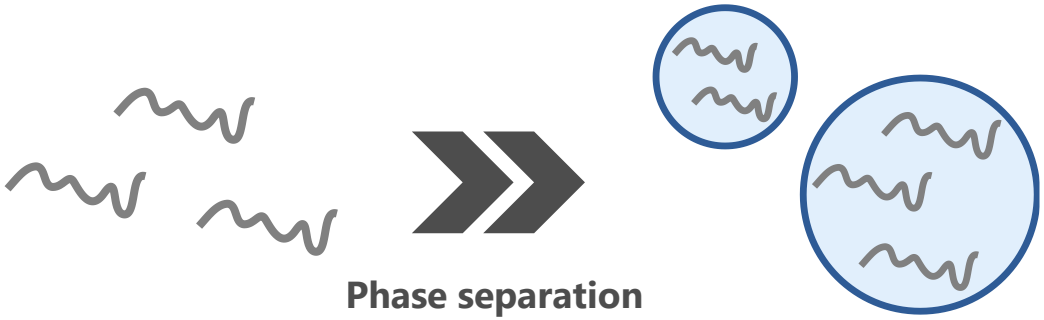

Monomer **Amyloid LLPS**

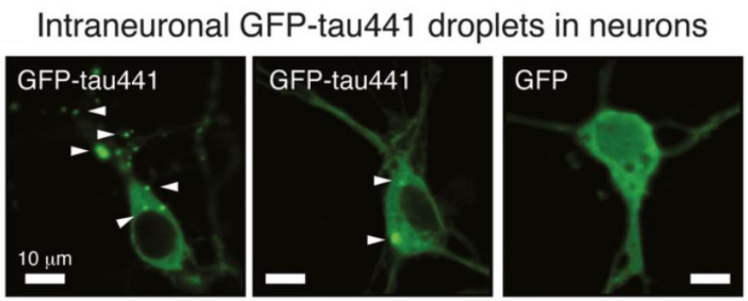

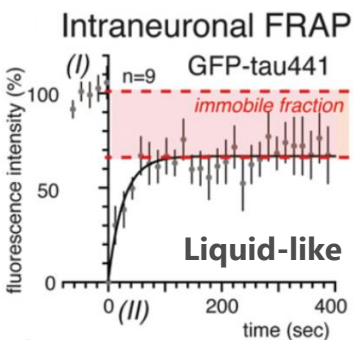

Primary cortical mouse neurons (初代皮質神経) expressed with GFP-tagged full-length tau (tau441)

S. Wegmann *et al.*, *EMBO J.*, **2018**, 37(7), e98049. B. Solomiia *et al.*, *PNAS.*, **2020**, 117(50), 1882-1890.

LLPS and disease

LLPS in amyloid aggregation process (abnormal)

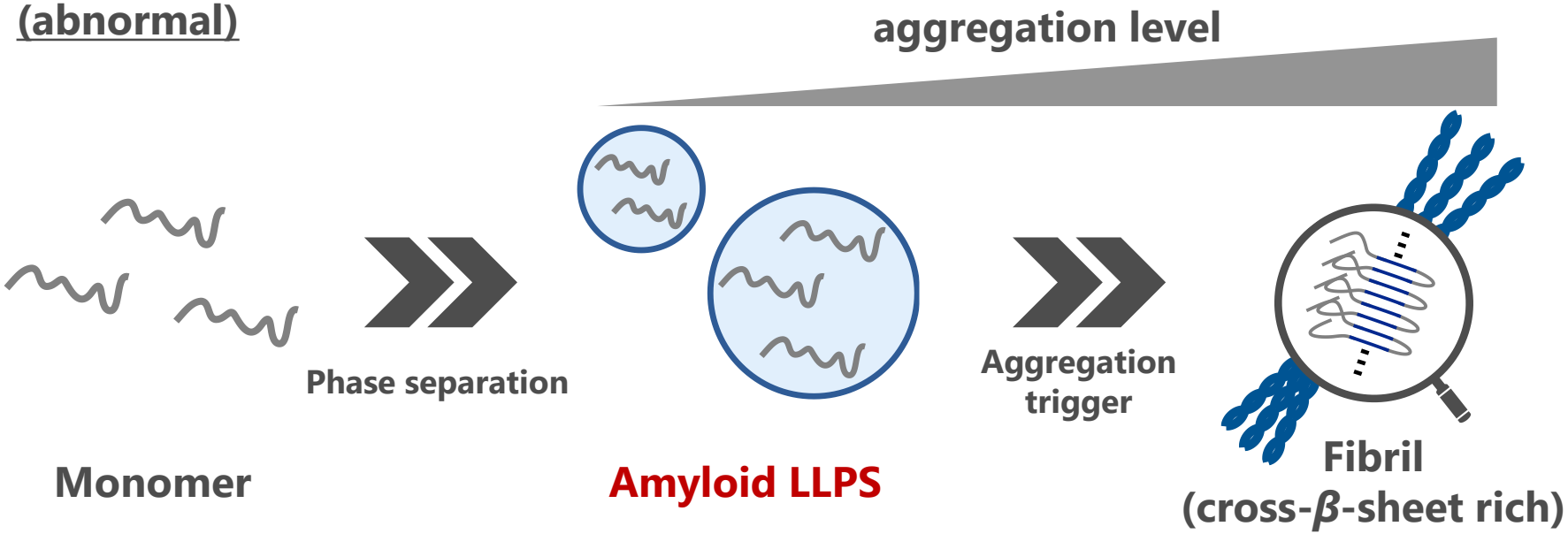

Intraneuronal GFP-tau441 droplets in neurons

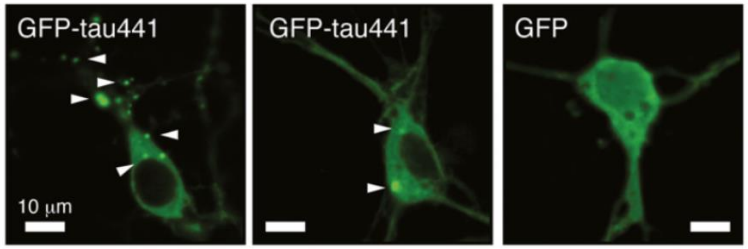

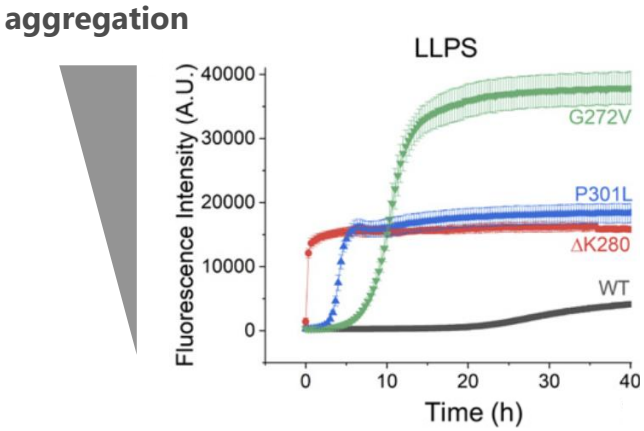

In vitro
ThT aggregation
assay

S. Wegmann *et al.*, *EMBO J.*, **2018**, 37(7), e98049. B. Solomiia *et al.*, *PNAS.*, **2020**, 117(50), 1882-1890.

LLPS and disease

Cancer

Transcriptional regulation by Super-enhancer (euchromatin)

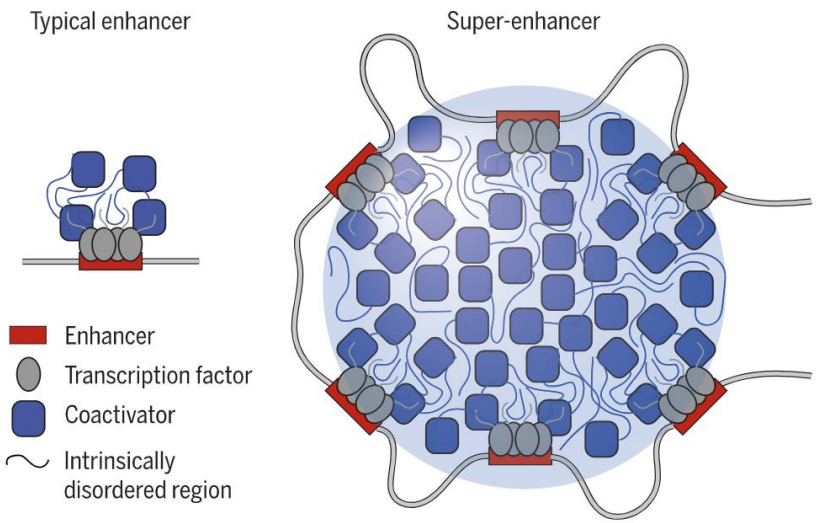

Dysregulation of LLPS in malignant cells

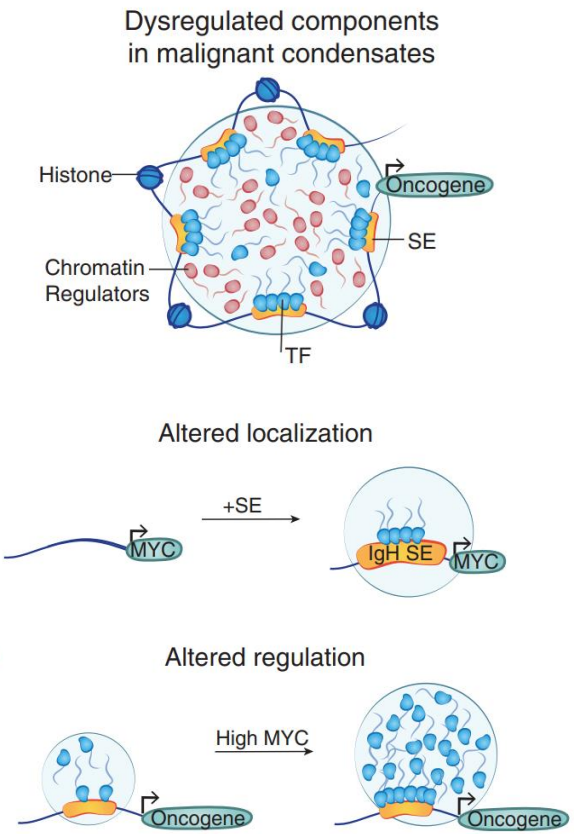

B. R. Sabari *et al.*, *Science*, **2018**, 361, eaar3958.

A. Boija *et al.*, *Cancer Cell*, **2021**, 39, 174-192.

LLPS and small-molecule therapeutics

Therapeutic small molecules concentrate in distinct intracellular environments

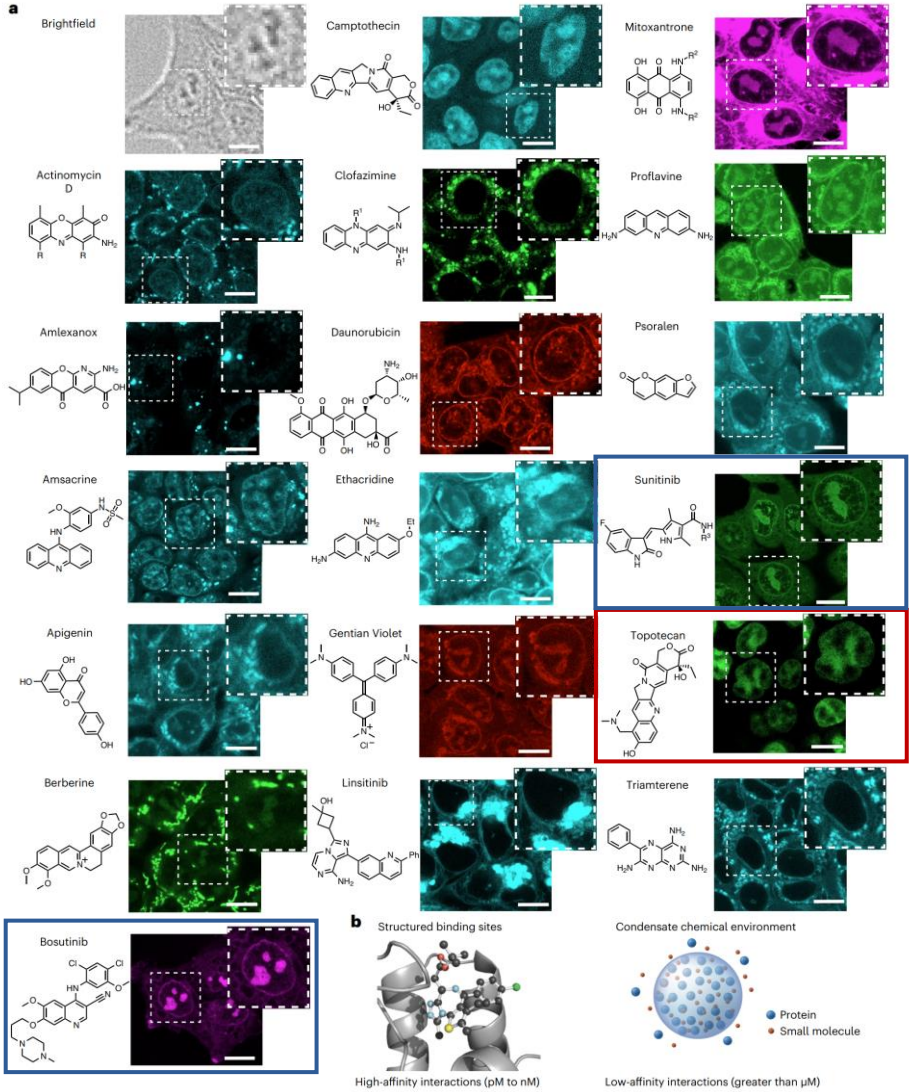

HCT-116 cells:
Human colorectal cancer 116 cells
(ヒト結腸直腸がん細胞)

Fig. 1 | Therapeutic small molecules concentrate in distinct intracellular environments. a, Micrographs showing live HCT-116 cells that were incubated with endogenously fluorescent drugs (50 μM) for 1 h and imaged with a confocal microscope. Dashed-line boxes indicate zoom (×2) cutout source, scale bar is 10 μm. R, Thr-D-Val-Pro-Sar-MeVal; R_1, *p*-chlorobenzene; R_2, $CH_2CH_2OCH_2CH_2NH_2$ and R_3, $CH_2CH_2N(CH_2CH_3)_2$. **b**, High-affinity protein–small molecule interactions can occur between a ligand and a structured ligand binding site, while weaker interactions with diverse features in the chemical environment of a condensate might independently concentrate small molecules in these macromolecular assemblies (Protein Data Bank ID 3mxf). These distinct interactions could work together to maximize the target engagement of a small molecule.

Sunitinib and Bosutinib:
anticancer receptor tyrosine kinase inhibitors
target: in the lipid bilayer and perhaps the cytoplasm
concentration: nucleoli (核小体) (membrane less organelle)

Topotecan:
Topoisomerase inhibitor
target: nucleus (核)
concentration: nucleus (核)

H. R. Kilgore *et al.*, *Nature Chemical Biology*, **2024**, 20, 291-301.

LLPS and small-molecule therapeutics

Drug resistance mechanism by LLPS

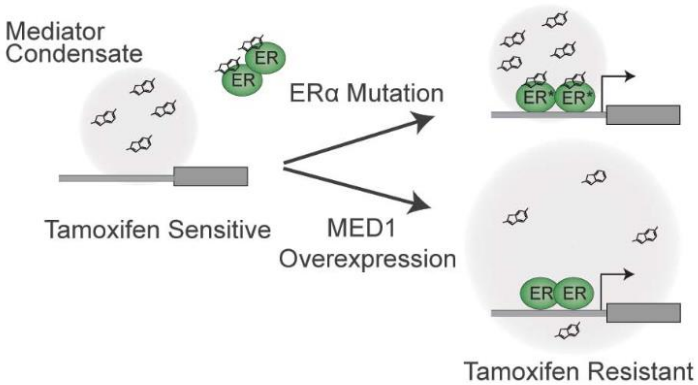

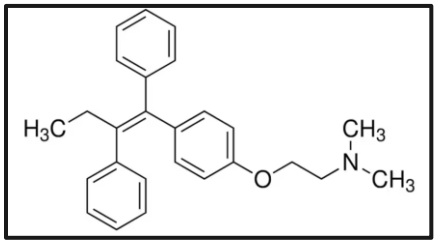

Tamoxifen: antineoplastic drug
(binding ER (Estrogen Receptor))

MED1: Subunit of Mediator
(transcriptional condensate-forming protein)

In breast cancer cells

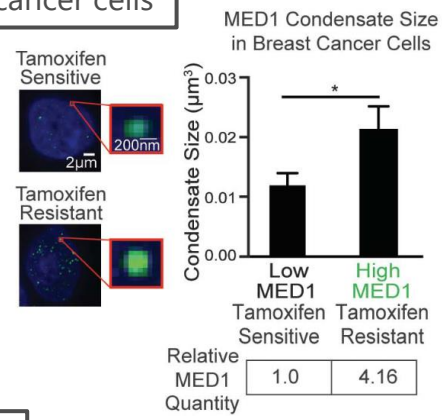

In vitro

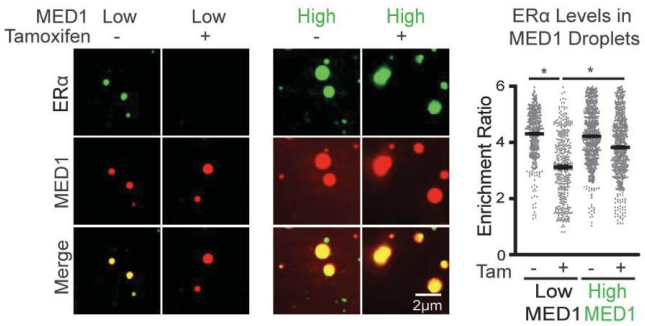

(**D**) In vitro droplet assays of ER in the presence of 100 μM estrogen with and without 100 μM tamoxifen with either 5 μM (low) or 20 μM (high) MED1. Droplets are formed with 5 μM ER in 125 mM NaCl and 10% PEG and imaged at 150× on a confocal fluorescent microscope. Error bars represent SEM.

I. A. Klein *et al.*, *Science*, **2020**, 368, 1386-1392.

LLPS and small-molecule therapeutics

Undesired therapeutics

Need of high dose
↓
cytotoxity and side effect

(c.f. Sunitinib, Bosutinib)

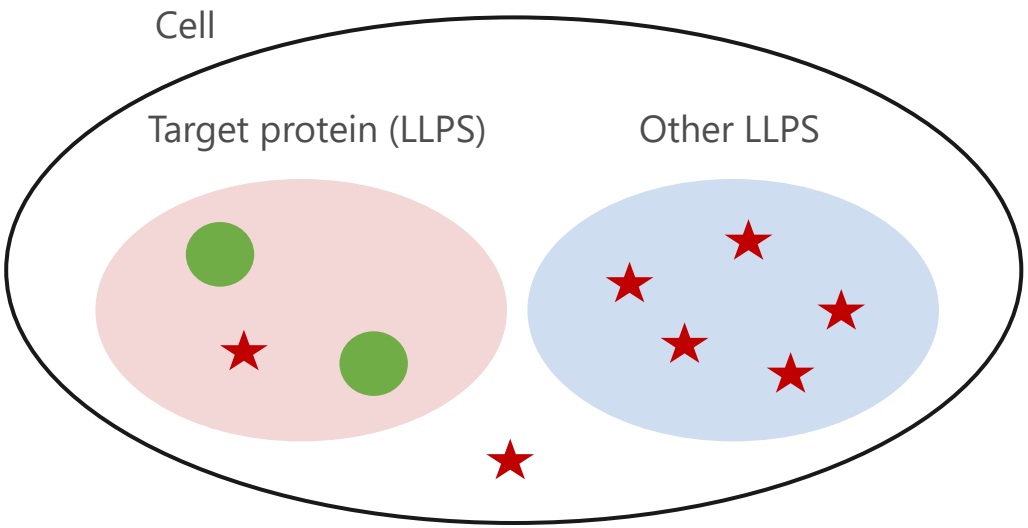

Desired therapeutics

Possibility of low dose
↓
less cytotoxity and side effect

(c.f. Tamoxifen)

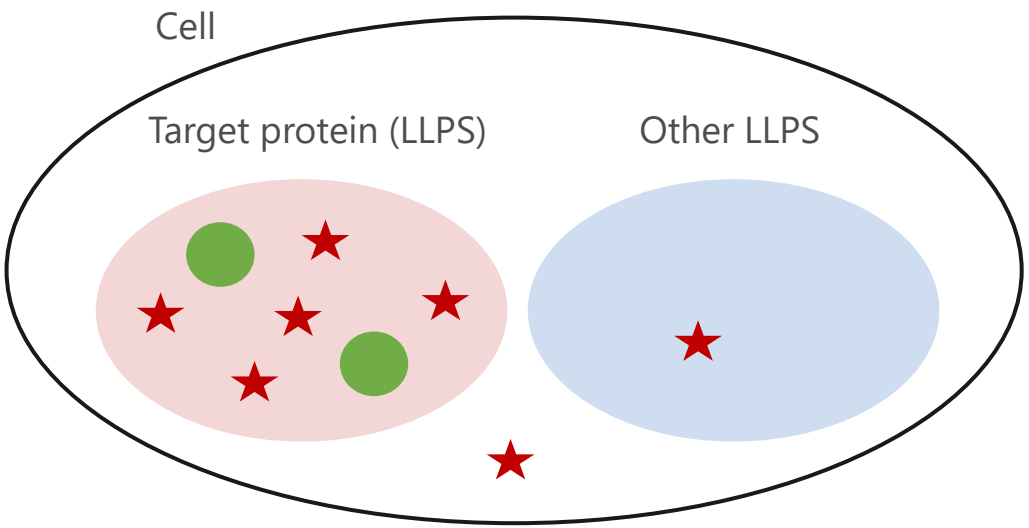

: target protein ★: small-molecule therapeutics

Table of contents

Chemical features and subcellular localization

Therapeutic small molecules concentrate in distinct intracellular environments

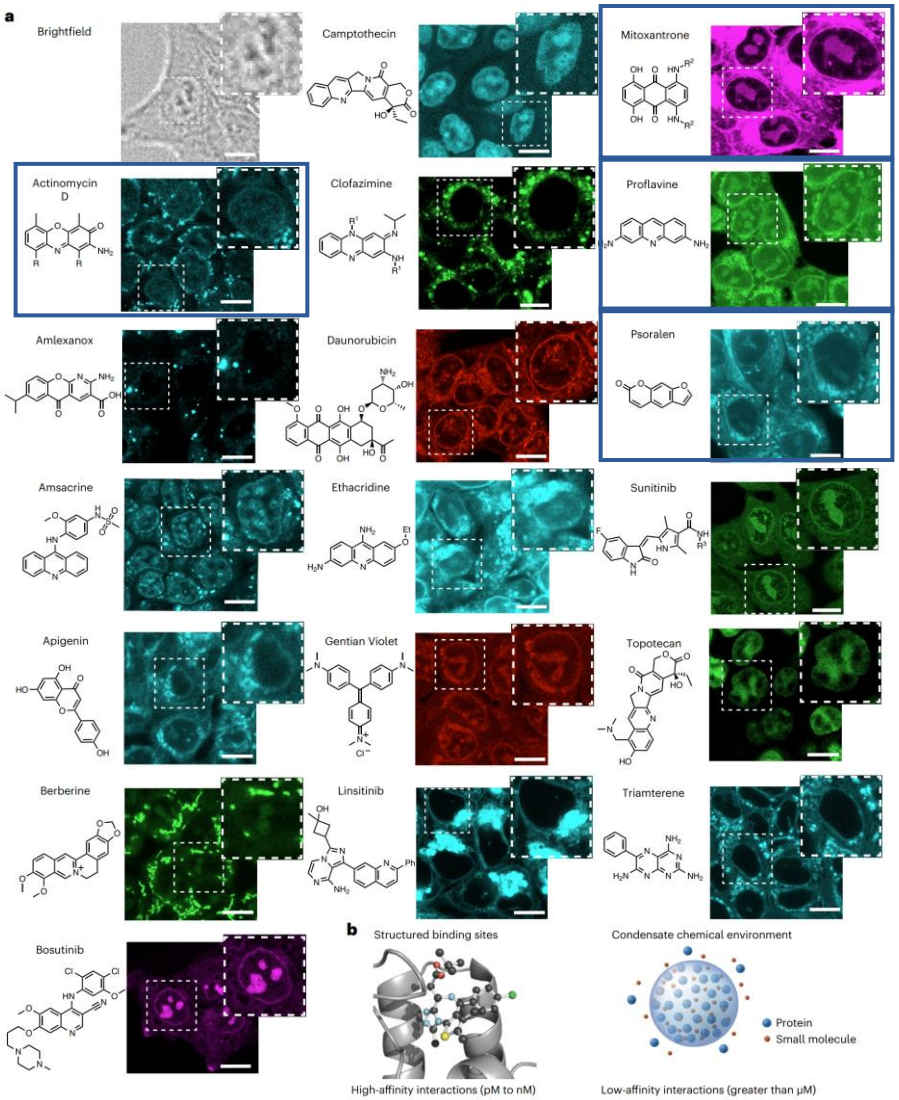

HCT-116 cells:
Human colorectal cancer 116 cells
(ヒト結腸直腸がん細胞)

Fig. 1 | Therapeutic small molecules concentrate in distinct intracellular environments. a, Micrographs showing live HCT-116 cells that were incubated with endogenously fluorescent drugs (50 μM) for 1 h and imaged with a confocal microscope. Dashed-line boxes indicate zoom (×2) cutout source, scale bar is 10 μm. R, Thr-D-Val-Pro-Sar-MeVal; R_1, *p*-chlorobenzene; R_2, $CH_2CH_2OCH_2CH_2NH_2$ and R_3, $CH_2CH_2N(CH_2CH_3)_2$. **b**, High-affinity protein–small molecule interactions can occur between a ligand and a structured ligand binding site, while weaker interactions with diverse features in the chemical environment of a condensate might independently concentrate small molecules in these macromolecular assemblies (Protein Data Bank ID 3mxf). These distinct interactions could work together to maximize the target engagement of a small molecule.

Actinomycin D, Mitoxantrone, Proflavine, Psoralen:
nucleic acid binding compounds

Different chemical features

↓

Different subcellular localization

H. R. Kilgore *et al.*, *Nature Chemical Biology*, **2024**, 20, 291-301.

In vitro condensate reconstitution

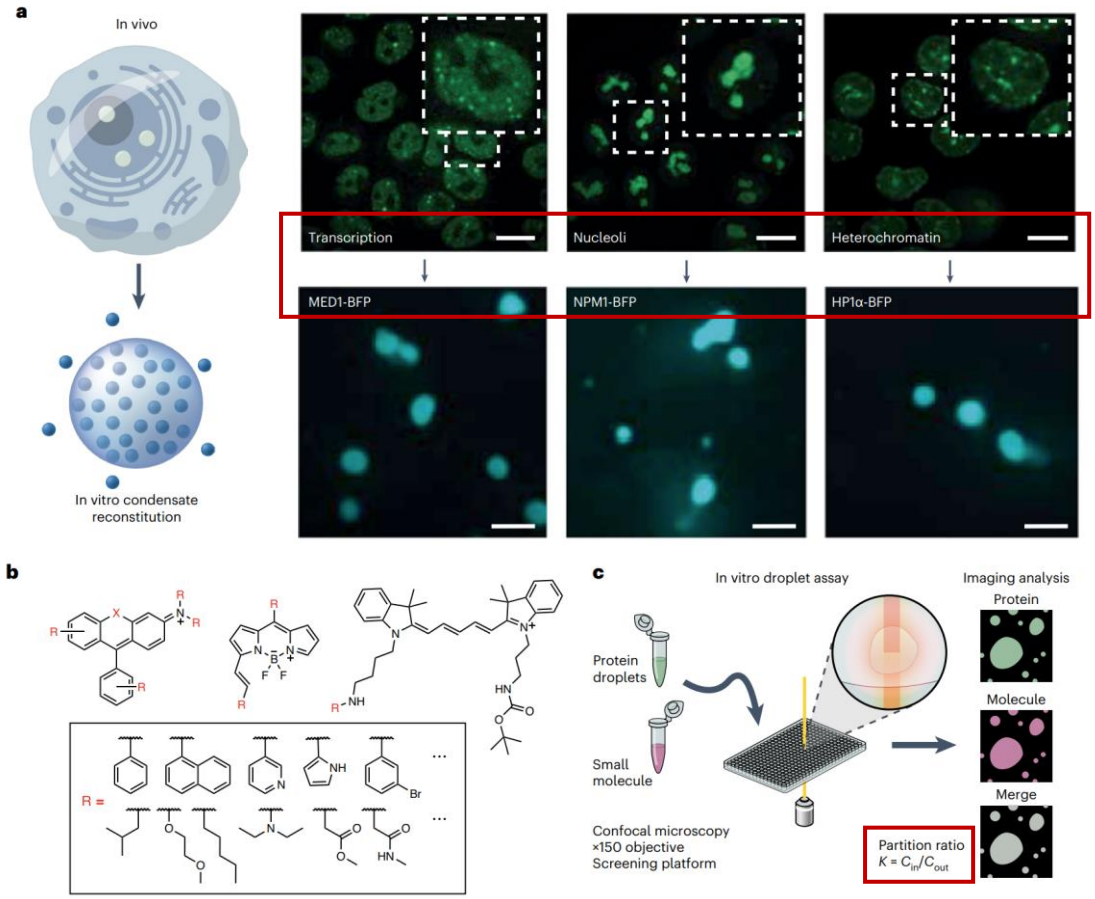

Fig. 2 | Selective partitioning of small molecules in simple condensates. **a**, Live cell condensate scaffold proteins can be reconstituted in vitro. Top, HCT-116 cells expressing MED1-GFP (transcriptional condensates), NPM1-GFP (nucleolar condensates) and HP1α -GFP (heterochromatin condensates). Bottom, homotypic in vitro condensates formed with indicated scaffold proteins fused to blue fluorescent protein (top scale bar, 10 µm, ×2.0 zoom and bottom scale bar, 2 µm). **b**, Chemical scaffolds of fluorescent probes used to measure partitioning within condensate assays and example R-groups. **c**, Schematic of the in vitro condensate partitioning screen and calculation of probe partition ratio, *K*. The screen was performed with 50 µM probe and 5 µM protein.

Small molecule fluorescent probe library

The small molecule fluorescent probe library consisted of a pool of 6,000 fluorescent dyes. The library consisted of xanthene, BODIPY and cyanine dyes. These dyes were prepared through combinatorial chemistry using a range of R-groups sampling a range of chemistry including: alkyl, alkenes, aromatic rings, sulfonamides, nitriles, N, S and O mono- and di-substituted heteroaromatic rings (five- and six-membered), alkyl, aryl and heteroaryl hydroxyl groups, alkyl, aryl and heteroaryl halogens, alkyl and aryl methoxy groups, alkyl and aryl ethoxy groups, alkyl substituted aromatic and heteroaromatic rings (five- and six-membered), alkyl, aryl and heteroaryl carbonyl compounds, 1,2,3-triazoles, primary amines, secondary amines, tertiary amines in linear and saturated carbocycles, esters, trichloroacetyl esters and trifluoroacetyl esters. Compounds were derivatized to incorporate a primary alkyl or aryl amine, alkyl or aryl acetamide, or an alkyl or aryl chloroacetyl moiety on the 5, 3 or 8 position of the BODIPY dye, and the 3, 6 or 9 position of xanthene dyes. Xanthene dye scaffolds consisted of rhodamine, rhodol, fluorescein, thioxanthene and N-substituted xanthenes. BODIPY probes were modified at the 5, 3 and 8 positions. Xanthene dyes were modified at 3, 6 and 9 positions of the ring. Cyanine dyes were modified at the heteroaromatic nitrogen atom and conjugated to a linker substituted with additional chemical motifs. Selection of probes for experiments was made by the fluorophore and microscope optical constraints. Fluorescent probes were maintained at a concentration of 10 mM in dimethylsulfoxide (DMSO) and stored at −80 °C.

Homotypic in vitro droplet assay

Recombinant MED1-IDR-BFP, HP1α-BFP and NPM1-BFP fusion proteins were purified and concentrated to 50 µM as described above.

Protein was added to a droplet formation buffer consisting of 50 mM Tris HCl, 1 mM DTT, 125 mM NaCl, 10% 8 kDa polyethylene glycol crowding agent at pH 7.5. A Tecan Evo 150 or a Beckman Echo 655 liquid handler was used to dispense 50 nl of fluorescent probe from a master plate containing fluorescent probes at 10 mM in DMSO, to a solution of 1 µl of 50 µM protein and 9 µl of droplet formation buffer as described above to provide a final probe and protein concentration of 50 and 5 µM, respectively. The plate was sealed with parafilm, protected from light and incubated at 37 °C overnight to equilibrate the sample. After equilibration, droplet images were recorded at room temperature using the plate screening mode with the Andor microscope as described above. In total, 11 images were recorded for each fluorescent probe at different locations within the image with 500 ms exposures and a normalized laser power.

H. R. Kilgore *et al.*, *Nature Chemical Biology*, **2024**, 20, 291-301.

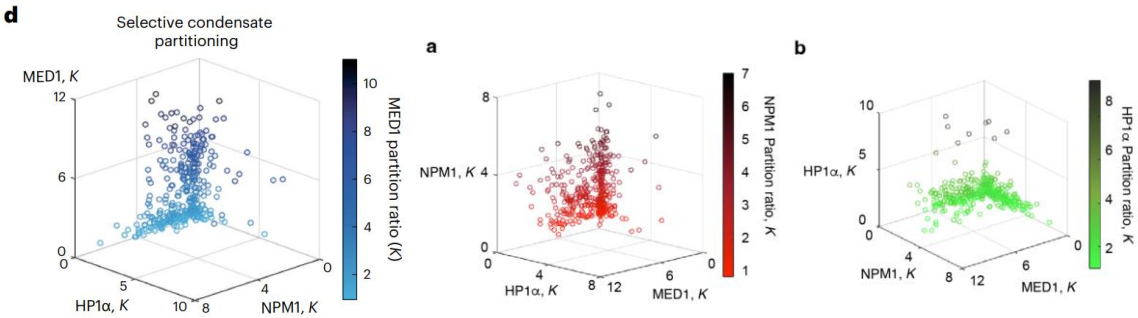

Fig. 2 | Selective partitioning of small molecules in simple condensates. **d**, Three-dimensional scatter plot of probes compared across condensates; color gradient is proportional to MED1 partition ratio. **e**–**g**, Dot plots comparing the partition ratio percentiles of the highest partitioning probes in MED1 (**e**), NPM1 (**f**) and HP1α condensates (**g**) (left distributions) to the percentiles of these probes in the other condensates (middle and right distributions), sample size $n = 50$ probes. Centerline and error bars represent mean ± s.d. (unadjusted P value, ****$P < 0.0001$, ***$P < 0.001$, **$P < 0.01$, *$P < 0.05$. P values calculated with a two-sided Wilcoxon matched-pairs signed rank test, test statistics $|W|$: 1,146, 1,162 (**e**), 1,148, 1,153 (**f**) and 1,166, 1,249 (**g**)).

Supplementary Figure 4. 3-D scatter plot of fluorescent probes compared across each condensate. a, NPM1 partition ratio (red to black), **b**, HP1α partition ratio (green to black). Color gradient is dictated by the probe's partition ratio in **a**, NPM1 and **b**, HP1α respectively.

Many probes were enriched in one or more condensates.

Partition ratio of each top 50 partitioning probes

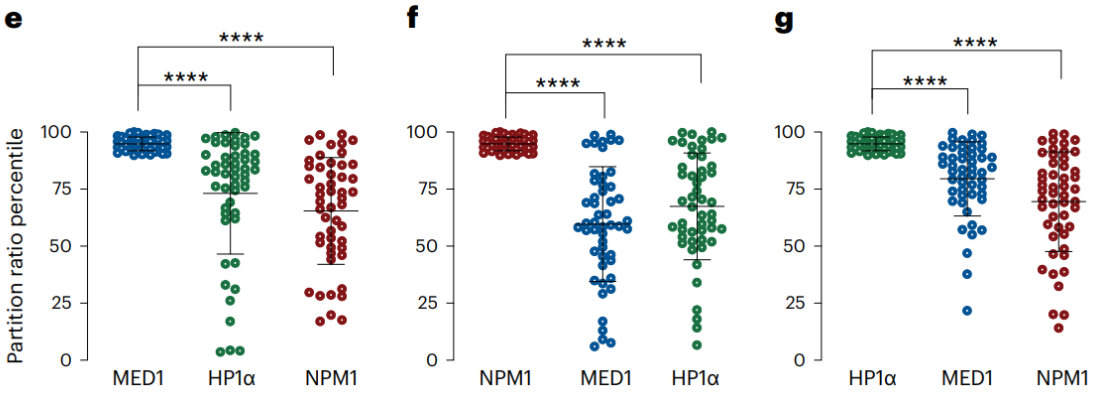

Droplet image analysis

Droplet image analysis was performed using an in-house developed Python script. In brief, a binary mask was generated from the 405 nm or protein channel signal that was of at least 25 pixels in size and with intensity values above the background of each image (droplets were detected from the 405 nm excitation channel). The intensity of the fluorescent probe was measured within and outside of the regions demarcated by this mask in the fluorescent probe channels (488, 561, 640 nm) and averaged. The concentration of a fluorescent probe was assumed to be proportional to the intensity of the fluorescent probe inside and outside of the binary mask, and the partition ratio, K, was computed as intensity $\cong C$, for $C = C_{in}$ or C_{out} as defined by the binary mask. The partition ratio used here is the quotient of these values $C_{in}/C_{out} = K$. The total number of probes used in MED1, NPM1 and HP1α droplets were 1,143, 1,055 and 963 molecules, respectively. Measurements of protein partition ratio were assessed by evaluation of the fluorescent signal intensity inside and outside of the mask using the 405 nm channel. Measurements of condensate circularity were performed using scikit-image measure package on the computed masks from the 405 nm channel.

The partition ratios of high-partitioning probes in these condensates were generally greater than the partition ratios in the other condensates.

H. R. Kilgore *et al.*, *Nature Chemical Biology*, **2024**, 20, 291-301.

Chemical similarity and partition ratio

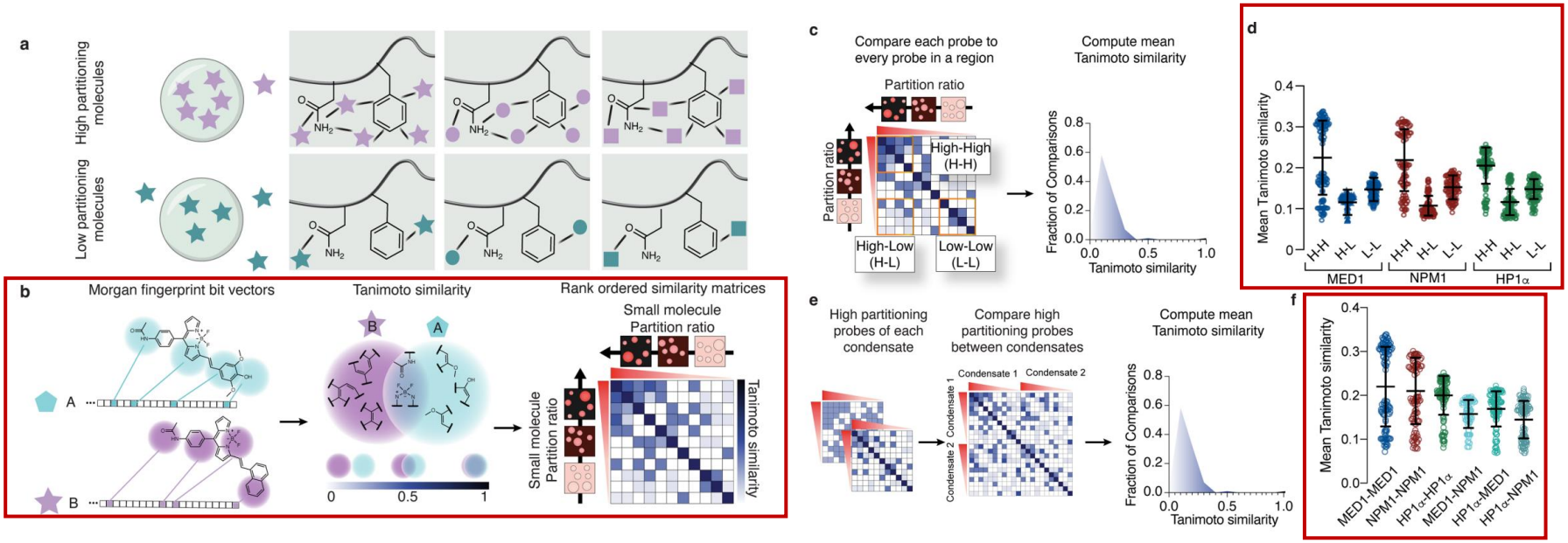

Extended Data Fig. 5 | Probe features suggest a chemical grammar in condensates. a, Cartoon depicting how similar molecules (here, sharing color) might interact with the same chemical environment. **b**, Schematic showing calculation of Tanimoto similarity matrices comparing fluorescent probes by their Morgan Fingerprints. **c**, Schematic and **d**, dot plots showing calculation of mean Tanimoto similarities from matrices of fluorescent probes compared against each other in high-to-high (H-H), high-to-low (H-L) and low-to-low (L-L) partitioning regions. **e**, Graphic and **f**, dot plots show the comparison of high partitioning probes between condensates through quantification of matrices, significance between groups was not assessed. Centerline and error bars represent mean ± s.d. Panel **d**, all comparisons were statistically significant with *P* value, $P < 0.0001$ (asterisks do not appear in figure), sample size MED1 $n = 120$. NPM1 $n = 100$. HP1α $n = 100$, without adjustment for multiple comparisons. Unpaired two-sided *t*-test statistic and degrees of freedom: MED1 H-H, $t = 9.5$, $df = 238$. MED1 H-L, $t = 12.7$, $df = 238$. MED1 L-L, $t = 7.3$, $df = 238$. NPM1 H-H, $t = 12.17$, $df = 198$. NPM1 H-L, $t = 7.4$, $df = 198$. NPM1 L-L, $t = 9.4$, $df = 198$. HP1α H-H, $t = 4.8$, $df = 198$. HP1α H-L, $t = 10.7$, $df = 198$. HP1α L-L, $t = 8.3$, $df = 198$.

Chemoinformatics
Fluorescent probe chemical structures were generated as SMILES strings and sanitized. Pairwise Tanimoto similarity calculations were performed using Morgan Fingerprints with a radius of 2 in a 2,048-bit depth as implemented in the program RDKit (v.2021.03.2)[28]. Calculations of log*P*, hydrogen bond acceptor count, number of rotatable bonds, topological polar surface area (TPSA) and molecular weight were computed with RDKit (v.2021.03.2)[28].

Tanimoto similarity classifiers
Tanimoto similarity classifiers were constructed from probes that had measured partition ratios in the 90th percentile of probe partitioning data for each condensate. These sets of probes were used to compute Tanimoto similarity metrics with other probes, drugs and natural products. Fluorescent probes that had computed Tanimoto similarities above various thresholds (0.50, 0.75, 0.80 and 0.85) were labeled as 'true' and those below these values were computed as 'false'. Natural products and drugs were classified using a Tanimoto similarity threshold of 0.5, above this threshold natural products and drugs were labeled as 'true' and below 'false'. These data were then plotted in a receiver operating characteristic curve (see Calculation of receiver operating characteristic curves for more details). Tanimoto similarity calculations were performed as described in the Chemoinformatics section.

Morgan fingerprint: presence (1) or absence (0) of a chemical feature
Tanimoto similarity: chemical similarity (molecular similarity)

A:	1	0	1	1	1	0	1	1	0	0	1	1
B:	0	0	1	1	0	0	1	0	1	0	1	1

$$c_{Tanimoto}(A, B) = \frac{n(A \cap B)}{n(A \cup B)} \quad (=5/9)$$

H. R. Kilgore *et al.*, *Nature Chemical Biology*, **2024**, 20, 291-301.

Success of deep learning prediction

Chemical feature

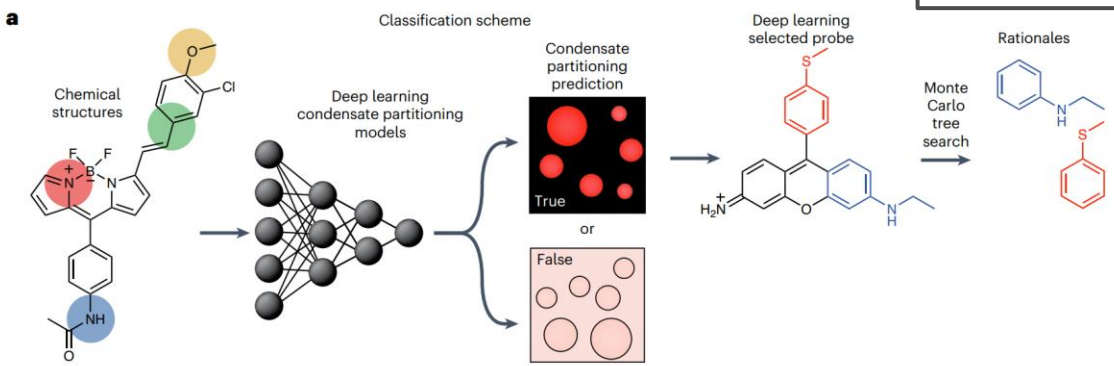

Fig. 3 | Deep learning discovers compounds with selective partitioning behaviors. a, Schematic of a MPNN for classifying probe partitioning behaviors into in vitro condensates and evaluation of their rationales. **b**, Bar graph showing the median partition ratio of deep learning (DL) and randomly selected probes (RS). **c**, Dot plots of partition ratio for fluorescent probes selected by DL or RS in MED1 (DL sample size $n = 56$, RS sample size $n = 224$ probes, $t = 6.6$, degrees of freedom (d.f.) = 278), NPM1 (DL sample size $n = 50$ probes, RS sample size $n = 240$, $t = 17.2$, d.f. = 288) and HP1α (DL sample size $n = 40$ probes, RS sample size $n = 240$ $t = 3.6$, d.f. = 278) in vitro condensate assays. Centerline and error bars represent mean ± s.d. **d**, Analysis of in vitro deep learning models, (left) bar graph depicting

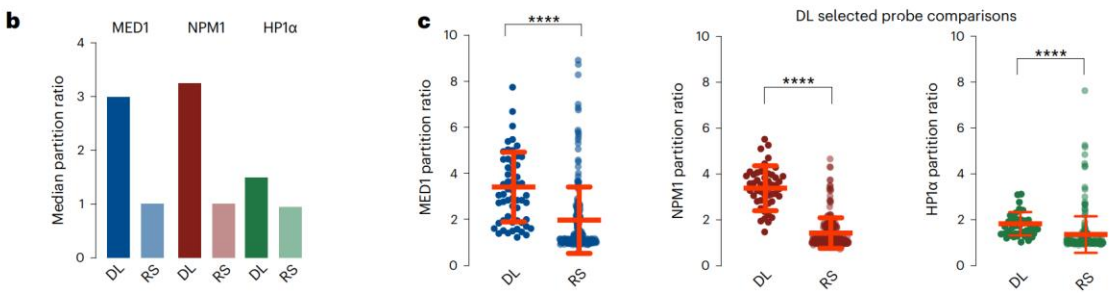

DL: Deep Learning
RS: Random Select

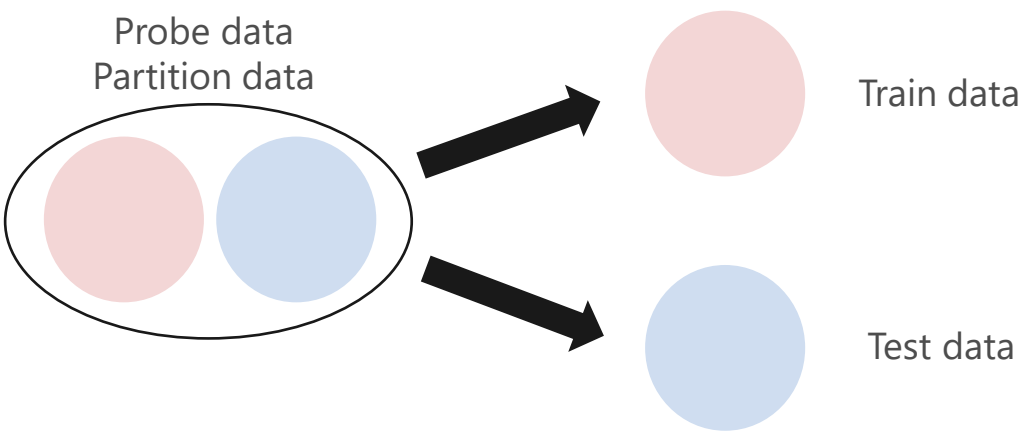

Compare to RS,
DL predicted probes
with high partitioning ratio.

H. R. Kilgore *et al.*, *Nature Chemical Biology*, **2024**, 20, 291-301.

Importance of cationic and aromatic motifs

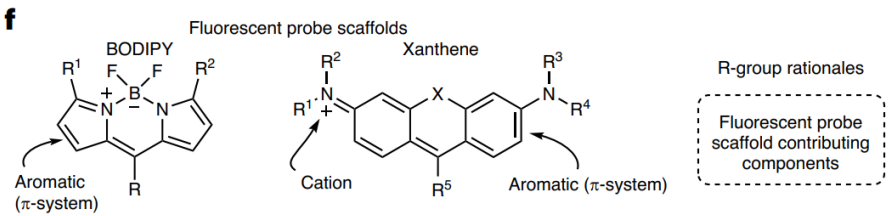

Fig. 3 | Deep learning discovers compounds with selective partitioning behaviors.

f, Chemical structures of fluorescent probe scaffolds. **g**–**i**, Rationales of fluorescent probe scaffolding (shown in box) and functional groups in MED1 (**g**), NPM1 (**h**) and HP1α condensates (**i**) (unadjusted *P* value ****$P < 0.0001$, ***$P < 0.001$, **$P < 0.01$, *$P < 0.05$, evaluated with a two-tailed *t*-test).

The probes predicted to partition into MED1, HP1α and NPM1 condensates were identified to be primarily xanthene and BODIPY that possess electron donating R-groups and electron rich π-system.

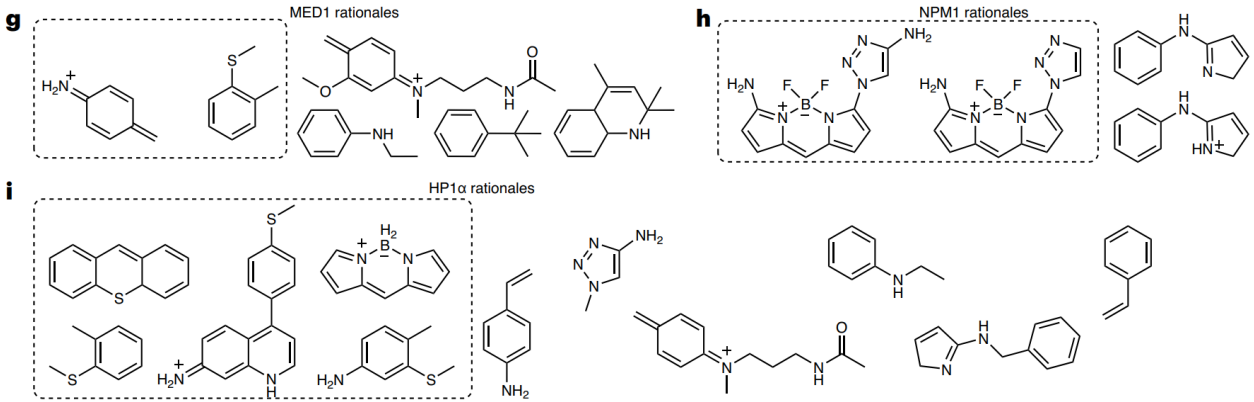

MED1 rationales: 1. **aromatic rings functionalized with electron donating, withdrawing and neutral motifs**
2. **cationic amines and their N-acetyl propylamine derivatives**

NPM1 rationales: 1. **aromatic and amine rich moieties, which compose the scaffold of BODIPY**

HP1α rationales: 1. **aromatic ring structures and building blocks of BODIPY and xanthene**

H. R. Kilgore *et al.*, *Nature Chemical Biology*, **2024**, 20, 291-301.

Live cell partitioning predicted by deep learning

Supplementary Table 2. Nucleolar and chromocenter enrichment compared against the NPM1 and HP1a deep learning classifier prediction of FDA drugs and natural products.

Drug	Nucleolar enrichment†	Deep learning Prediction of NPM1 partitioning†	Tanimoto Prediction of NPM1 partitioning§	Chromocenter enrichment‡	Prediction of HP1α partitioning‡	Tanimoto Prediction of HP1α partitioning*
Actinomycin D	No	True	False	No	False	False
Amlexanox	No	True	True	No	False	True
Amsacrine	Yes	True	True	No	False	False
Apigenin	No	False	False	No	False	False
Amiloride	No	False	False	No	False	True
Baicalein	Yes	False	False	No	False	True
Bedaquiline	No	False	False	No	False	False
Berbamine	Yes	False	False	No	False	False
Berberine	Yes	False	False	No	False	False
Bosutinib	Yes	False	False	No	False	False
Broxyquinoline	No	False	False	No	False	False
Camptothecin	Yes	False	False	No	False	False
Cinchonidine	No	False	False	No	False	False
Clofazimine	No	False	False	No	False	False
Daunorubicin	No	False	False	Yes	False	True
Diacerein	No	False	False	No	False	False
Dibucaine	No	False	False	No	False	False
Epalrestat	No	False	False	No	False	False
Ethacridine	Yes	True	True	No	False	False
Etretinate	No	False	False	No	False	False
Gentian Violet	Yes	False	False	No	False	False
Isorhamnetin	No	False	False	No	False	False
Kaempferol	No	False	False	No	False	False
Linsitinib/OSI-906	No	True	True	No	False	False
Mitoxantrone	Yes	True	True	Yes	True	True
Piperine*	No	False	False	No	False	False
Proflavine	Yes	True	True	Yes	True	True
Psoralen	Yes	False	False	No	False	False
Quinine	No	False	True	No	False	False
Rutin	No	False	True	No	False	False
Scutellarin	No	False	True	No	False	False
Simeprevir	Yes	False	False	No	False	False
Sunitinib	Yes	False	False	Yes	True	True
Suramin	No	True	True	No	True	False
Tanshinone I*	No	False	False	No	False	False
Tanshinone II*	No	False	False	No	False	False
Triamterene	No	True	True	No	False	False
Tryptanthrin	No	False	False	Yes	True	True
Topotecan	Yes	False	False	No	False	True
Wedelolactone	No	False	False	No	False	False
XL765	Yes	True	False	No	False	False

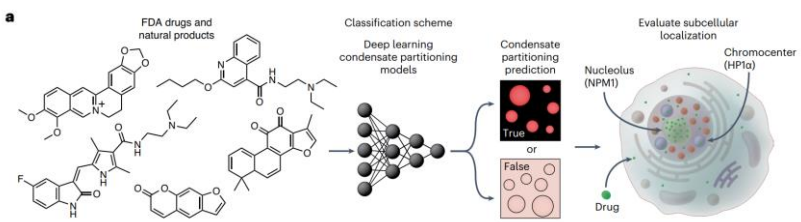

Heterochromatin region

Fig. 4 | Live cell partitioning predicted by deep learning classifiers. **a**, Schematic of approach for identifying molecules that concentrate in live cell condensates from in vitro parititoning models. Small molecules were evaluated for in vitro partitioning behavior and then compared to their live cell imaging

A true positive (TP) is defined, Nucleolar / chromocenter enrichment = yes and prediction of NPM1/ HP1α = True.

A false positive (FP) is defined, Nucleolar / chromocenter enrichment = NO and prediction of NPM1/ HP1α = True.

A true negative (TN) is defined, Nucleolar / chromocenter enrichment = NO and prediction of NPM1/ HP1α = False.

A false negative (FN) is defined, Nucleolar / chromocenter enrichment = yes and prediction of NPM1/ HP1α = False.

†Analysis of the NPM1 deep learning model and experimental results (Table S2) provided the following inputs, TP = 5, FP = 5, FN = 10, and TN = 21.

‡Analysis of the HP1α deep model and experimental results (Table S2) provided the following inputs, TP = 4, FP = 1, FN = 1, TN = 35.

§Analysis of the NPM1 Tanimoto calculation and experimental results (Table S2) provided the following inputs, TP = 4, FP = 7, FN = 11, and TN = 19.

*Analysis of the HP1α Tanimoto calculation and experimental results (Table S2) provided the following inputs, TP = 5, FP = 4, FN = 0, TN = 32

NPM1: 10 drugs predicted to concentrate in nucleoli (DL with vitro data)
5 were observed to do so and
31 drugs predicted not to concentrate in nucleoli,
11 appeared to concentrate in nucleoli.

HP1α: 5 drugs predicted to concentrate in chromocenters (DL with vitro data)
4 were observed to do so and
36 drugs predicted not to concentrate in chromocenters,
1 appeared to concentrate in chromocenters.

DL, trained on simple in vitro condensates, could predict that some drugs will selectively concentrate in the more complex environment of the relevant condensates in cells, albeit with limited accuracy.

H. R. Kilgore *et al.*, *Nature Chemical Biology*, **2024**, 20, 291-301.

Table of contents

Summary

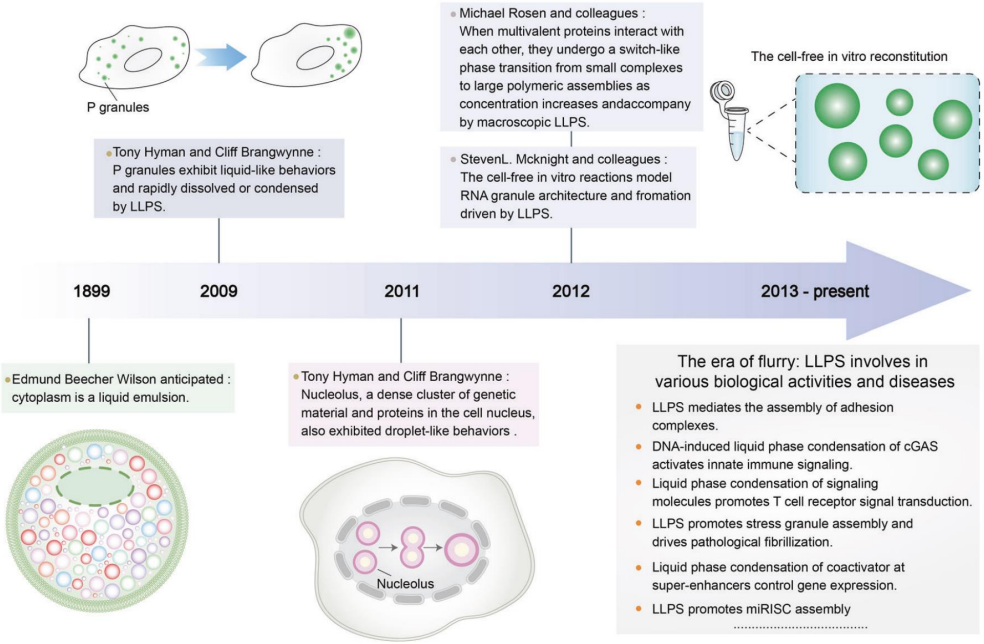

New era

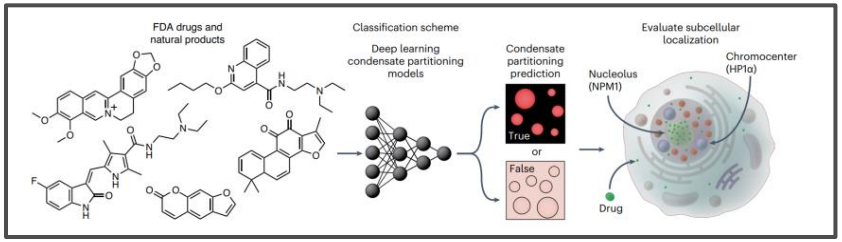

- **Prediction of molecular localization in LLPS with deep learning**
- **LLPS and disease, therapeutics**

Table of contents

Post Translational Modification (PTM)

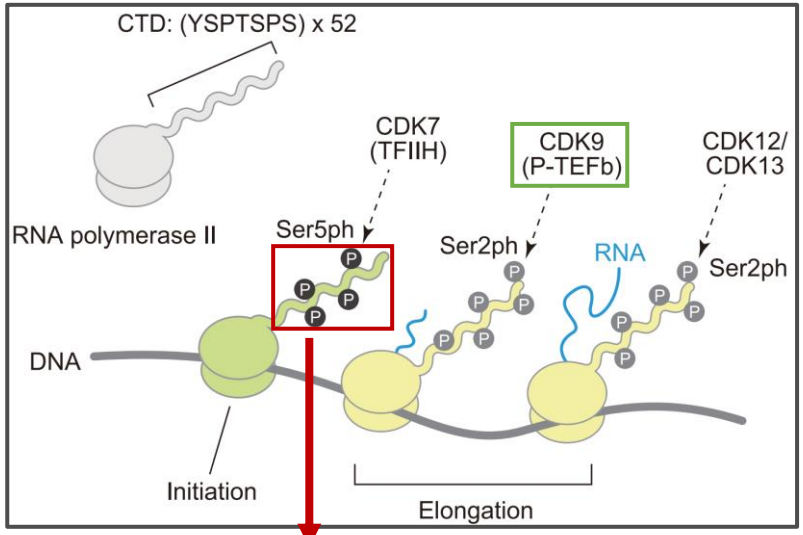

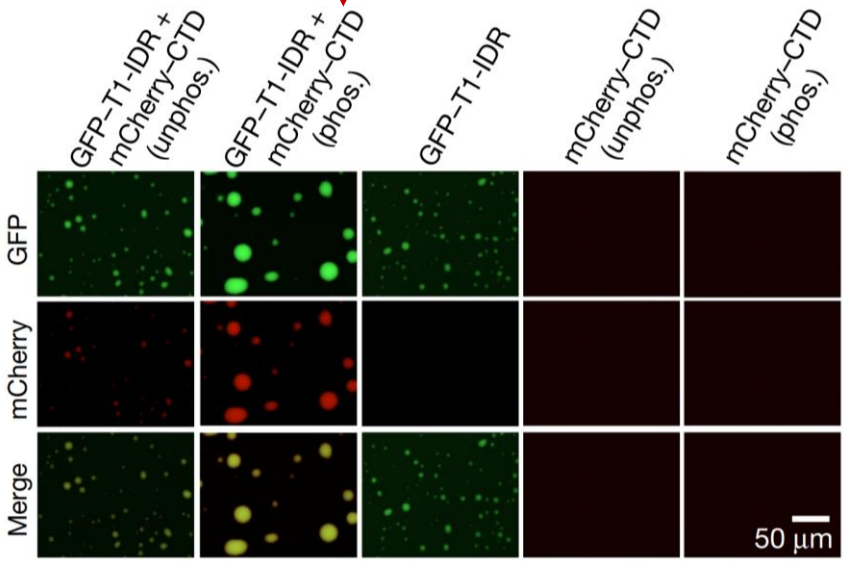

P-TEFb (Positive Transcription Elongation Factor b): consisting of CDK9 and cyclin T1 (CYCT1)

In vitro
20 mM Tris-HCl (pH7.5), 1 mM DTT, 37.5 mM NaCl, 6 mg/mL protein solutions

T1-IDR (Histidine rich):
IDR (491-686) of transcription-related cyclin T1 (CYCT1)
CTD (phos. type: use of CDK7):
C-terminal domain (YSPTSPS x52) of RPB1 subunit of human RNA polymerase II(RNAPII)

H. Kimura and Y. Sato, *Current Opinion in Cell Biology*. **2022**, 74, 71-79. H. Lu *et al.*, *Nature*. **2018**, 558(7709), 318-323.

LLPS and small-molecule therapeutics

Cisplatin

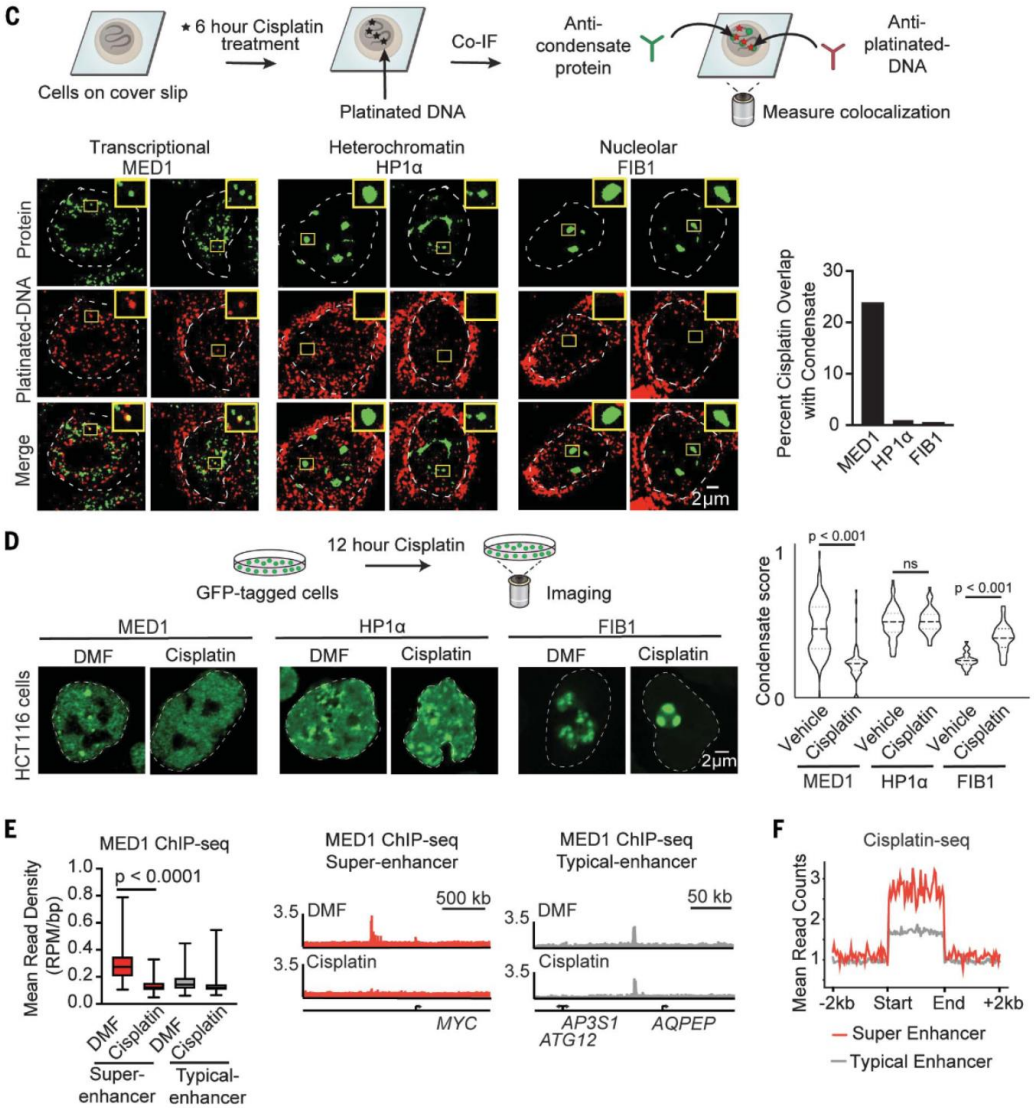

I. A. Klein *et al.*, *Science*, **2020**, 368, 1386-1392.

LLPS and small-molecule therapeutics

Therapeutic small molecules concentrate in distinct intracellular environments

Supplementary Table 1. Subcellular distribution of endogenously fluorescent FDA drugs and natural products.

Drug	Dominant Staining Pattern	Suggested targets	Subcellular localization	Comments
Actinomycin D	Cytoplasmic	DNA TopI/TopII complexes[1-4] SH2[5]	[6,7]	-
Amiloride	Cytoplasmic	Na^+/H^+ transporters [8,9] Nucleic acids[10] Diamine oxidase[11] Adenosine receptors Andrenoreceptors[12] Muscarinic recpetors[13]	-	-
Amlexanox	Cytoplasmic punctate	TBK1 [14] IKK-epsilon[14] S100A4[15] S100A13[16] Phosphodiesterase 4B[17] IKBKE[18]	-	Review of anticancer activity[19]
Amsacrine	Nuclear	DNA TopI/TopII complexes[20,21]	-	-
Apigenin*	Mitochondrial	DNA[22] OAT1[23] Ribosomal protein S9[24]	-	Broad activity[25,26] Antioxidant activity[27]
Baicalein*	Cytoplasmic punctate	DNA[28] MAP4K3[29] TLR4[30] Lysozyme[31] RAF-1[32] Platelet lipoxygenase[33]	-	-
Bedaquiline	Cytoplasmic	ATP synthase[34] Membranes[35,36]	[37,38]	-
Berbamine*	Cytoplasmic	STAT3 [39] NF-κB [40]	-	Signaling modulation[41-45]
Berberine*	Mitochondrial and Nuclear	KCNH6 potassium channel [46] NEK7[47]	[48]	Broad activity[49,50]
Bosutinib	Nucleolar	Bcr-Abl[51] Global kinase profile[52]	-	-
Broxyquinoline	Cytoplasmic punctate	ACBP1 [53] Cellular metals[54]	-	-
Camptothecin	Nuclear	DNA and TopI complex [55] hnRNP A1[56]	[57]	An insightful review on topoisomerase pharmacology [58]
Cinchonidine	Cytoplasmic	Sodium channel[59] Butyrylcholinesterase [60]	-	Cinchona alkaloid pharmacology[61]
Clofazimine	-	RKIP [62] eIF6-60S ribosome [63]	[64,65]	Anti-microbial[66] thought to bind mycobacterial DNA, and affect respiration and membrane integrity [67]
Daunorubicin	-	DNA [68] DNA TopII complexes[58,69]	[70-76]	Chemotherapeutic [77], DNA intercalator, DNA TopII poison [58,69]
Diacerein	Cytoplasmic	Cytochrome P450 2C9[78]	-	Interleukin-1 beta inhibitor with effects on multiple signaling pathways, including STAT3, MEK/ERK, FAK[79-81]
Dibucaine	Cytoplasmic	Spectrin[82] Na^+ / Ca^{+2} channels[83,84]	-	Local anesthetic[85], Calmodulin antagonist[86]
Epalrestat	Cytoplasmic	Aldose reductase [87]	-	Aldose reductase inhibitor [88]
Ethacridine	Cytoplasmic	DNA[89,90]	[91]	Endomicroscopy applications[92,93]
Etretinate†	Cytoplasmic	Retinol binding protein[94]	-	Synthetic retinoid[95]
Gentian Violet	Nuclear	Nucleic acids [96] Acetylcholinesterase [97]	[98]	Anti-microbial [99 100] Inhibits NADPH oxidase and thioredoxin system [101]
Isorhamnetin	Cytoplasmic	Catalase [102] MEK1 [103], PI3K [103] PPARG [104] ERK [103]	-	Broad Activity [105]
Kaempferol*	Cytoplasmic	Calcineurin [106] PI3K [107] VEGF [108] PD1/PD-L1 [109] multidrug resistance protein [110] LXR [111]	-	Broad activity[112-116]
Linsitinib/OSI-906	Cytoplasmic	Insulin receptor, IGF-1R [117 118]	-	Tyrosine kinase inhibitor [119]
Mitoxantrone	Cytoplasmic Nucleolar	Nucleic acids [120,121] FAK [122] PIM [123]	[124,125]	DNA-TopII poison and other targets [126]
Piperine*	Cytoplasmic	ACAT [127] cytochrome P4501A1 [128] Myosin regulatory light chain[129] DHODH [130] HSP70 [131]	-	Alkaloid present in black pepper [132]
Proflavine	Nuclear	Nucleic acids [133,134] Rev[135]	[91]	-
Psoralen	Cytoplasmic	Double-stranded DNA (crosslinking) [136] ErbB2[137]	-	Applications towards transcriptome analysis[138]
Quinine	Cytoplasmic	Fe(II)-protoporphyrin IX[139] Cocaine binding aptmer[140] Debrisoquine 4-hydroxylase[141] Purine nucleoside phosphorylase[142]	-	Sirt3 PI3K/Akt/FoxO3a signaling[143] General properties of alkaloids[81]
Rutin*	Cytoplasmic	Carbonyl reductase [NADPH] 1[144]	-	Broad activity[145] Antioxidant activity[146]
Scutellarin*	Cytoplasmic punctate	AKT 1/2[147] Nrf2[148]	-	Broad activity[149]
Simeprevir	Cytoplasmic Nuclear	NS3/4A Protease[150]		Hepatitis C[151]
Sunitinib	Nuclear	Multiple kinases[152] ABC transporters[153] K^+ transporters[154] PDGF-receptor[152,155] Flt3[155]	[156,157]	Development of molecule[158]
Suramin	Cytoplasmic	-	-	Broad Activity[159]
Tanshinone I*	Cytoplasmic	-	-	Broad Activity[160]
Tanshinone II*	Cytoplasmic	-	-	Broad Activity[160,161]
Triamterene	Cytoplasmic	VEGF165[162] Ion channels[163] Myocardial beta-receptor[164]	-	Diuretic[165]
Tryptanthrine	Nuclear	-	-	Broad Activity[166]
Topotecan	Nuclear	DNA and TopI complex[167,168]	[57]	-
Wedelolactone*	Cytoplasmic	IKK complex[169]	[170]	Antioxidant activity[171,172] Broad activity[171,173-176]
XL765	Cytoplasmic	PI3K/mTOR[177,178]	-	-

* Traditional medicines

† Recalled from the market

Broad activity is noted for compounds that have been reported to modulate numerous biochemical processes

H. R. Kilgore *et al.*, *Nature Chemical Biology*, **2024**, 20, 291-301.

LLPS and small-molecule therapeutics

- **Therapeutic small molecules concentrate in distinct intracellular environments (two-photon imaging for ultraviolet region excitation)**

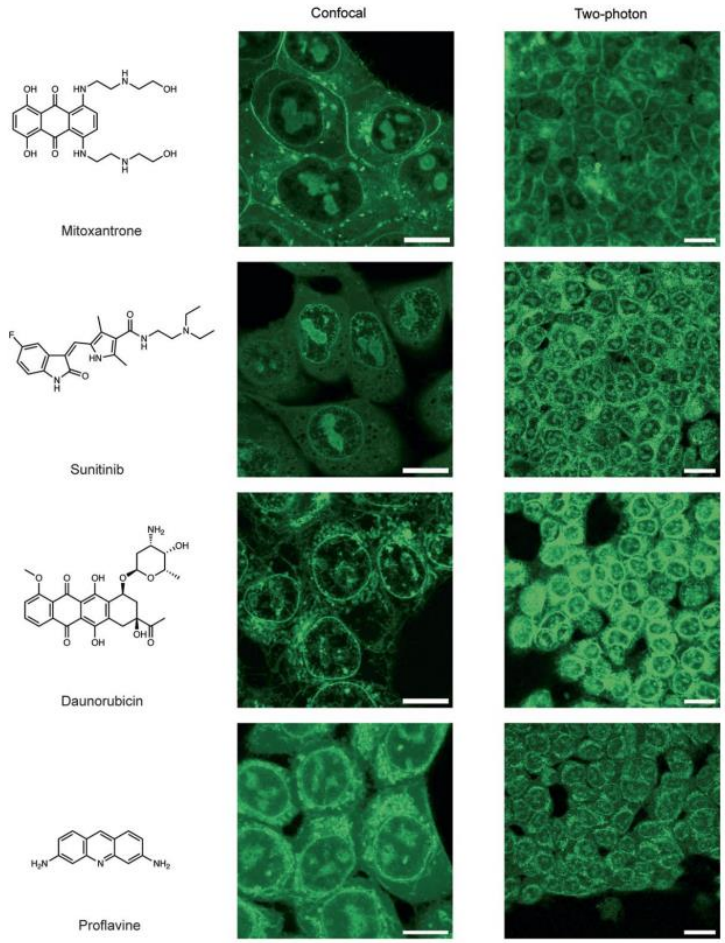

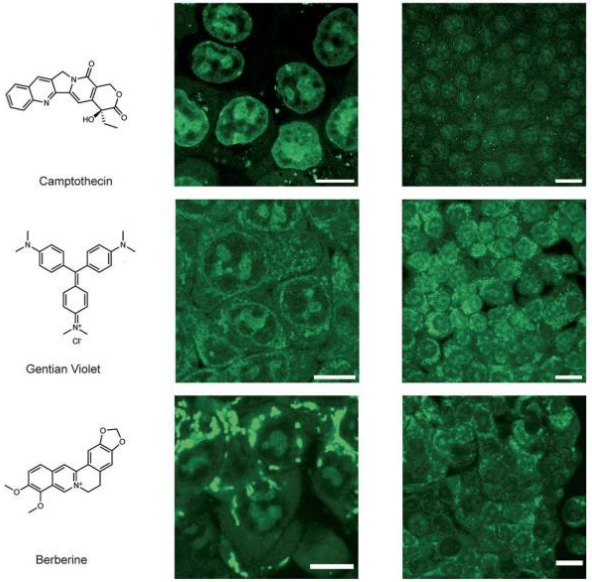

Extended Data Fig. 1 | Live cell confocal and two-photon imaging of endogenously fluorescent drugs. HCT-116 cells were incubated with a drug or natural product at 50 μM for 1 hour and then imaged with a confocal or two-photon microscope. Image for sunitinib is also shown in Fig. 1. Scale: 10 μm.

H. R. Kilgore *et al.*, *Nature Chemical Biology*, **2024**, 20, 291-301.

Small molecule-protein interactions in condensates

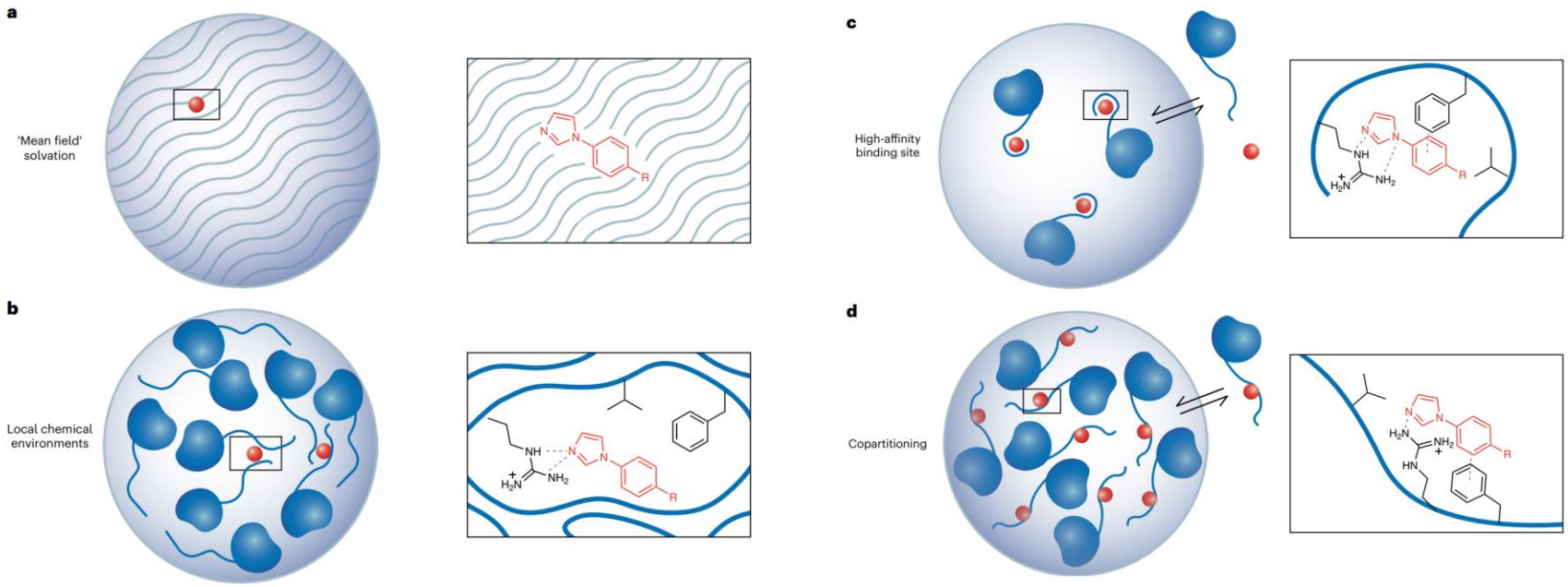

Fig. 5 | Small molecule–protein interactions in condensates. Internal chemical environments in condensates selectively concentrate small molecules. **a**, Internal chemistries of condensates could concentrate molecules simply by differing in classical bulk phase properties (for example, dielectric constant). **b**, Association of polymers could lead to the creation of local chemical environments or 'chemical pockets' that concentrate small molecules. **c**, Concentration of a protein into a condensate could lead to changes in the ensemble of states occupied by a biopolymer, creating a high-affinity small molecule binding site. **d**, Small molecules and proteins could bind through the same structures inside and outside a condensate, such that increase in protein concentration inside of the condensate effectively concentrates the small molecule.

H. R. Kilgore *et al.*, *Nature Chemical Biology*, **2024**, 20, 291-301.

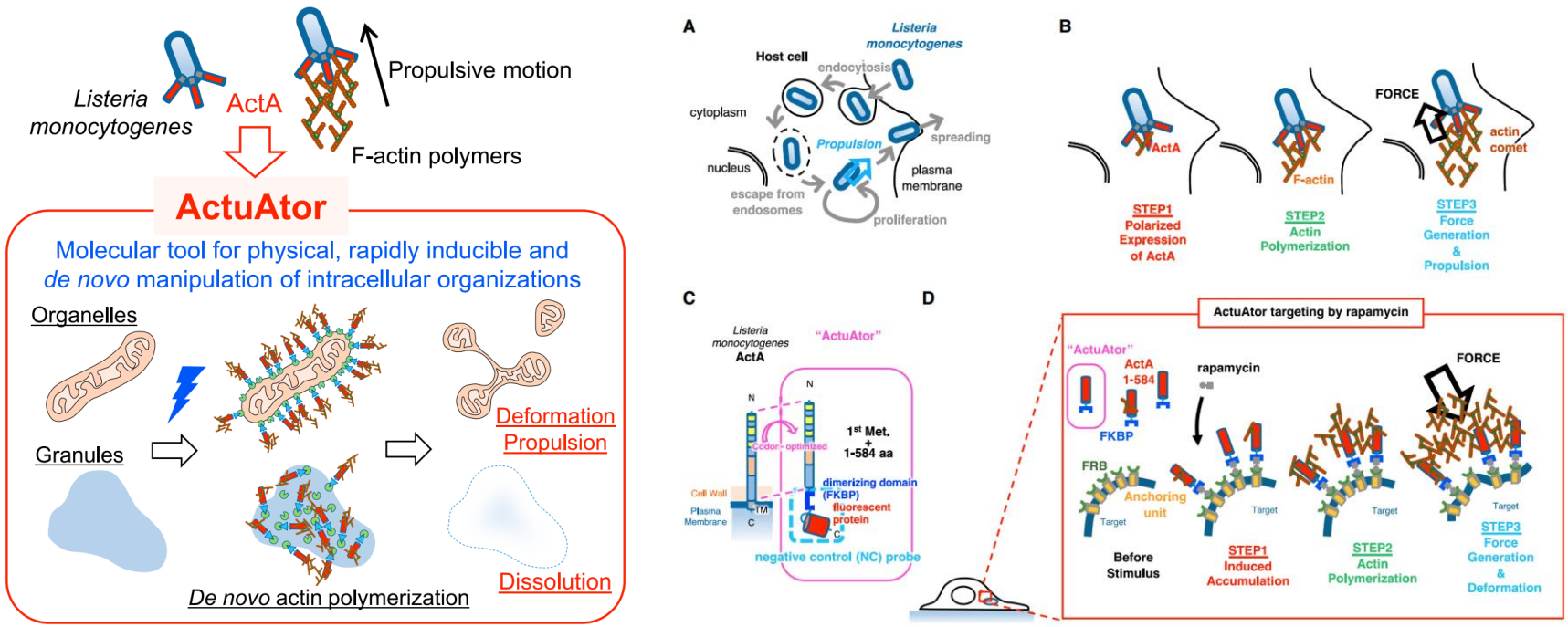

Figure 1. A novel tool, ActuAtor, was developed based on a bacterial protein ActA

(A) Life cycle of *Listeria monocytogenes* in host cells. *Listeria* invades into the cytosol by endocytic entry into host cells followed by escape from endosomes. They proliferate in the cytosol and move around by hijacking actin polymerization of the host cell. The propulsion process is essential for the bacteria to escape from the host cell to spread across other cells in the tissue.

(B) Mechanism of *Listeria* propulsion in the host cell cytosol. A bacterial membrane protein, ActA, is essential for the process. In the host cell cytosol, *Listeria* expresses ActA in a polarized manner (left panel). Extracellular domain of ActA then induces polymerization of host cell actin by functionally mimicking actin nucleation promoting factors of the host cell (middle panel). The polymerized actin polarization generates directional force exerted onto the bacteria, propelling them in the cytosol to realize bacterial motion (right panel).

(C) Schematic drawing of the engineered peptide, termed ActuAtor, derived from ActA. Extracellular domain of original ActA was codon-optimized for mammalian expression and was fused to a dimerizing domain (blue) and a fluorescent protein (red). An NC peptide that lacks the ActA-derived domain (NC probe, highlighted by cyan broken line) was used in the following experiments. Basic characterization of ActA-derived domain, including actin polymerization-inducing ability, was performed *in vitro* and *in cellulo* (Figure S1).

(D) Design of a novel force-generating tool, ActuAtor. An engineered peptide depicted in (C) was accumulated onto the target, leading to actin polymerization that generates force.

H. Nakamura *et al.*, *Cell Reports*, **2023**, 42, 113089.